Wind turbine load validation in wakes using wind field reconstruction techniques and nacelle lidar wind retrievals

Davide Conti[1], Vasilis Pettas[2], Nikolay Dimitrov[1], and Alfredo Peña[1]

[1]Department of Wind Energy, Technical University of Denmark, Frederiksborgvej 399, 4000 Roskilde, Denmark
[2]Stuttgart Wind Energy (SWE), University of Stuttgart, Allmandring 5b, 70569 Stuttgart, Germany

Correspondence: Davide Conti (davcon@dtu.dk)

Abstract. This study proposes two methodologies for improving the accuracy of wind turbine load assessment under wake conditions by combining nacelle-mounted lidar measurements with wake wind field reconstruction techniques. The first approach consists ~~in~~ of incorporating wind measurements of the wake flow field, obtained from nacelle lidars, into random, homogeneous Gaussian turbulence fields generated using the Mann spectral tensor model. The second approach imposes wake deficit time-series, which are derived by fitting a bivariate Gaussian shape function on lidar observations of the wake field, on the Mann turbulence fields. The two approaches are numerically evaluated using a virtual lidar simulator, which scans the wake flow fields generated with the Dynamic Wake Meandering (DWM) model~~.~~, i.e., the *target* fields. The lidar-reconstructed wake fields are then input to aeroelastic simulations of the DTU 10 MW wind turbine ~~and the resulting load predictions are compared with loads obtained with the *target* (no lidar-based) DWM simulated fields. The accuracy of load predictions is estimated across a variety of lidar beam configurations, probe volume sizes, and atmospheric turbulence conditions. The results indicate that the 10-min power and fatigue load statistics~~for carrying out the load validation analysis. The power and load time-series, predicted with lidar-reconstructed fields, ~~are comparable with results obtained with the DWM simulations. Furthermore, the simulated power and load time-series~~ exhibit a high ~~level of~~ correlation with the ~~*target* observations, thus~~decreasing corresponding *target* simulations; thus, reducing the statistical uncertainty (realization-to-realization) inherent to engineering wake models such as the DWM model. We quantify a reduction in power and loads' statistical uncertainty by a factor between 1.2 and 5, ~~compared to results obtained with the *baseline*, which is DWM simulated fields with different random seeds~~depending on the wind turbine component, when using lidar-reconstructed fields compared to the DWM model results. Finally, we show that the ~~spatial resolutions of~~ amount of lidar-scanned points in the inflow and the ~~lidar's scanning strategies as well as the~~ size of the lidar probe volume are critical aspects for the accuracy of the reconstructed wake fields, power, and load predictions.

1 Introduction

Wind turbines operating under wake conditions experience higher loading ~~conditions~~ and lower power productions ~~compared to~~ than those operating under wake-free conditions (Barthelmie et al., 2009; Larsen et al., 2013). The wake-induced velocity deficit and its ~~spatial displacement, also referred to as wake meandering ,~~ meandering are critical aspects in both loads and power analyses (Madsen et al., 2010; Doubrawa et al., 2017). The former reduces the inflow wind speed and causes unbalanced aerodynamic load distribution at the rotor, which in turn induces high load cycle amplitudes in the whole wind turbine structure (Lee et al., 2012)~~, whereas the~~ . The latter is the main source of wake added turbulence (Madsen et al., 2010), affecting wind turbine responses and inducing high fatigue damage (Larsen et al., 2013). Moreover, small turbulence eddies that result from the breakdown of the tip vortices can cause small fatigue load cycles (Madsen et al., 2005). Thus, aeroelastic analysis of wind turbines operating under wake ~~condition requires a~~ conditions requires detailed modeling of the wake flow fields.

~~For the purpose of load validation~~To date, detailed predictions of wake-generated turbulence can be achieved with large eddy simulation (LES); however, the computational cost is prohibitive when large number of simulations are required. This makes engineering wake models a practical alternative for certain applications. For design load evaluation, the IEC 61400-1 standard (IEC, 2019) recommends the Dynamic Wake Meandering (DWM) model, among other low-order engineering wake models~~, which ensures low computational effort and an acceptable level of accuracy.~~ .

The DWM model ~~is a low fidelity physical model, recommended by the IEC standard, which simulates wind field time series including wake deficits together with a stochastic meandering model. The motions of the wake deficits are super-imposed~~ considers wakes to act as passive tracers displaced in the lateral and vertical directions by the large eddies of the atmospheric flow (Madsen et al., 2010). The wake field is modelled as a 'cascade' of quasi-steady velocity deficits emitted by the source turbine that meander through a pre-calculated stochastic meandering path and that are advected in the stream-wise direction adopting Taylor's hypothesis of frozen turbulence. These wake deficit time series are superposed on random three-dimensional turbulence fields serving as input for aeroelastic simulations ~~. The wake characteristics~~ (Larsen et al., 2008; Madsen et al., 2010) .

The wake flow features simulated by the DWM model are conditional ~~both on~~ on both the ambient conditions, which can be measured from a local meteorological mast, and the operational conditions of the upstream wind turbines. In order to carry out load simulations, the 10-min statistical properties (mean and variance) of the simulated ambient ~~and operational conditions~~ inflow are set to match the measured ambient wind statistics (Dimitrov and Natarajan, 2017). ~~However, since the synthetic turbulence realization, as well as the wake meandering, are~~

There are three primary sources of uncertainty intrinsic of engineering wake models that affect the accuracy in power and load predictions, which we here denote as the measurement, modeling and statistical uncertainty. The measurement uncertainty includes deviations between the measured quantity of interest (e.g., the ambient wind field's characteristics or the power and load data) and their actual true values.

The modeling uncertainty originates from the simplistic flow modeling assumptions adopted to describe wake flow fields. This type of uncertainty can partly be reduced by improving the wake model (e.g., by adding further physical effects) (Keck et al., 2015)

or by calibrating model parameters using measurements (Larsen et al., 2013; Reinwardt et al., 2020). Calibrating the DWM model with site-specific observations improves the accuracy in power and load estimates; however, such calibrations do not hold at other sites (Madsen et al., 2010; Keck et al., 2012; Larsen et al., 2013; Reinwardt et al., 2020). As a result, DWM model-based power and load assessments might be highly uncertain at a given site unless high spatial and temporal resolution measurements of the wake are available for model calibration.

The statistical uncertainty derives from the traditional method of performing aeroelastic simulations, for which the numerical wind fields are set to match the statistical properties (mean and variance) of the observed wind field on a 10-min basis. Since the numerical turbulence field and the wake meandering are stochastic processes, the instantaneous velocities of the simulated wake wind field and the resulting load prediction time-series are ~~not synchronized with the true~~ uncorrelated with the observations. This can lead to simulation errors (Zwick and Muskulus, 2015) and introduces high statistical uncertainty on power and load predictions (Dimitrov and Natarajan, 2017; Pedersen et al., 2019). Further, ~~statistics from a large set of simulations are required to compensate for the large load variations.~~ to accurately reconstruct wake meandering time series, it is essential to ensure accurate power and load predictions in a load validation analysis.

Alternative load verification procedures are being explored to potentially reduce the statistical and modelling uncertainty of engineering wake models ~~, as well as to~~ and replace measurements from masts with those from Doppler lidars ~~(Dimitrov et al., 2019; Reinwa~~ (Dimitrov et al., 2019; Reinwardt et al., 2020; Conti et al., 2020b). Lidars can provide high spatial and temporal resolution inflow observations and extend (and eventually replace) traditional point-like measurements such as those from cup and sonic anemometers. Further, as modern wind turbines have considerably increased in size, reaching rotor diameters of the order of 150–200 m, accurate measurements of the inflow wind field for aeroelastic calculations require multi-point and multi-height wind measurements within the entire rotor plane.

In particular, nacelle-mounted lidars have the advantage ~~to be~~ of being aligned with the rotor, which increases the amount of validation data in contrast to a fixed mast where only a small wind direction sector is valid. The feasibility of nacelle-mounted lidar observations has been demonstrated for wake characterization (Trujillo et al., 2011; Fuertes et al., 2018; Herges and Keyantuo, 2019; Reinwardt et al., 2020), lidar-assisted control (Schlipf et al., 2013; Simley et al., 2013, 2018), and power and load analysis in ~~freeestream~~ free-stream conditions (Wagner et al., 2014; Dimitrov et al., 2019).

The recent work of ~~Conti et al. (2020a) demonstrated that~~ Conti et al. (2020b) proposed a lidar-based load validation procedure ~~in~~ under wake conditions that describes wake flow fields by means of time-averaged wind field characteristics estimated using nacelle lidar measurements. Although the quantified uncertainty in lidar-based power and load predictions was found comparable to estimates from IEC-recommended practices that uses the DWM model (Conti et al., 2020b), the authors stated that lidar-based load validation procedures in wakes should account for a model of the wake deficit and its ~~dynamics~~meandering dynamics to predict power and load accurately.

Overall, developing lidar-based power and load validation procedures under wakes can improve monitoring wind turbine performance (Tautz-Weinert and Watson, 2017; Schreiber et al., 2020), reduce uncertainty in load predictions and lifetime estimations (Rommel et al., 2020), enhance power curve testing in wind farms (Lydia et al., 2014; Wagner et al., 2015), and develop wind turbine and wind farm control strategies (Bossanyi et al., 2014; Simley et al., 2018).

The present work proposes two alternative approaches for wind turbine load validation under wake conditions using nacelle-mounted lidar measurements combined with wake wind field reconstruction techniques. The first approach builds on the work of Dimitrov and Natarajan (2017), which incorporates multiple lidar retrievals in a turbulence field generated using the Mann spectral model (Mann, 1994) through a constrained Gaussian field algorithm. Incorporating nacelle-lidar measurements as constraints into turbulence fields can circumvent the DWM model's assumption to consider wakes as passive tracers (Madsen et al., 2010), while reconstructing the actual observed inflow at a high spatial and temporal resolution.

The second approach reconstructs wake deficit characteristics ~~and their motions~~ including wake meandering by fitting a bivariate Gaussian shape function on lidar retrievals and superimposes these deficits on a random realization of the Mann turbulence field. This approach intends to minimize errors in wake deficit representations and introduce the observed wake meandering path directly in the simulations. Both lidar-based wake field reconstruction techniques can potentially decrease the modeling and statistical uncertainty inherent to the DWM model, thus predicting accurate power productions and loads.

We evaluate these ~~methods on a numerical study~~ lidar-based wake field reconstruction techniques on a tailored-designed numerical framework that simulates a nacelle-mounted lidar scanning the synthetic wake ~~flow~~ fields generated with the DWM model. ~~Thus, we carry out aeroelastic simulations of the DTU 10 MW wind turbine (Bak et al., 2013) with the lidar-reconstructed fields, and evaluate the accuracy of load predictions against results obtained with the *target* non lidar-based DWM simulated fields. In this study, we make use of two sets of independent turbulence seed realizations to quantify the statistical uncertainty of load predictions inherent of the DWM model.~~ The main objective of this study is to verify that ~~,~~ nacelle-mounted lidar measurements incorporated into wake field reconstruction methods improve the accuracy of power and load predictions when compared to ~~the *target* loads, the load prediction obtained using lidar-reconstructed wake flow fields is as accurate or superior than that obtained with the DWM model using turbulence parameters matching the measured ambient wind statistics, which is the standard *baseline*~~wake field reconstruction using engineering wake models alone.

The work is structured as follows. In Sect. 2, we briefly formulate the load validation procedure. Section 3 introduces the methodology including the Mann spectral tensor model (Sect. 3.1) and the DWM model (Sect. 3.2). Section 3.3 describes the virtual lidar simulator and the analyzed scanning configurations. The wake field reconstruction techniques are formulated in Sect. 3.4. The results are provided in Sect. 4, including the uncertainty analysis of the lidar-reconstructed fields in ~~relation to the target wake fields in~~ Sect. 4.1, a detailed analysis of the load validation results in Sect. 4.2, and the sensitivities of the lidar specifications, e.g., probe volume size and sampling frequency, and those related to the atmospheric inflow conditions on the load predictions accuracy in Sect. 4.3. The last two sections are dedicated to the discussion of the findings and the conclusions from the study.

2 Problem formulation

The design load cases (DLCs) and load verification procedure for wind turbines operating in wakes are described in the IEC standards ~~(IEC, 2015, 2017, 2019)~~(IEC, 2015, 2019). The present work covers the analysis of fatigue loads of wind turbines operating in wakes (see IEC 61400-1, DLC1.2). ~~Following the approach of Dimitrov and Natarajan (2017), we~~ We apply the

one-to-one load validation procedure of the IEC 61400-13 (IEC, 2015), which consists of comparing simulated and targeted (e.g., measured) load statistics to assess the accuracy of aeroelastic simulations. As we carry out the load validation analysis numerically, we define a tailored-designed load validation procedure, inspired by the approach of Dimitrov and Natarajan (2017) and illustrated in Fig. 1. The DTU 10 MW wind turbine (Bak et al., 2013) is used as reference in this study.

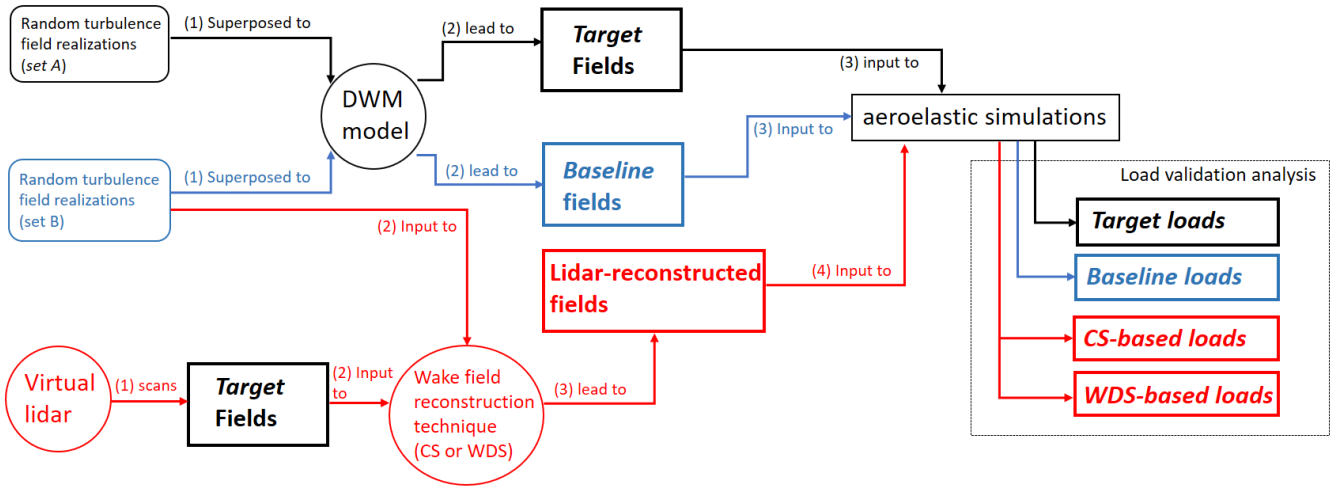

Figure 1. An illustration of the numerical framework utilized to reconstruct wake fields through the DWM model and our proposed lidar-based wake field reconstruction techniques (i.e., the constrained simulations CS and the wake deficit simulations WDS). Further, this framework allows quantifying the uncertainty in power and load predictions resulting from aeroelastic simulations with the DWM model-based and lidar-based wake fields. More details can be found in the text.

We use two sets of random turbulence ~~realizations (also referred to as seeds)~~field realizations, which we denote as *set A* and *set B*. ~~We simulate DWM-based~~ These turbulence fields are generated using the model by Mann (1994); thus, they are defined as zero-mean, homogeneous, uniform-variance Gaussian random fields. We simulate DWM model-based wake fields using turbulence ~~seeds~~ realizations from *set A*, which we denote as the *target* fields ~~. We also generate a second set of DWM-based~~ (see the black rectangular box in Fig. 1).

In contrast, the DWM model-based wake fields using ~~seeds~~ turbulence field realizations from *set B* ~~, which we denote as~~ are denoted as the *baseline* ~~. Since~~ (see the blue rectangular box in Fig. 1). Since the turbulence fields from *set A* and *set B* ~~come from the same distributions~~ have the same turbulence characteristics, as they are generated using the same Mann parameters but are statistically independent ~~,~~ (i.e., the resulting wind fields time series are uncorrelated), we expect that the outcomes of load simulations with *set A* and *set B* will have the same statistical properties ~~,~~ but will not be correlated ~~.~~ (Dimitrov and Natarajan, 2017).

Hence, the result of a one-to-one comparison of load statistics between the ~~realizations in the~~ *baseline* and the *target* simulations is a direct measure of the statistical uncertainty (i.e., load scatter) that originates from both the random Mann-based turbulence realizations and the stochastic meandering process ~~.~~ inherent to the DWM model. In a traditional load validation

analysis, the *target* loads will be the measured loads, whereas the *baseline* loads will be the loads resulting from aeroelastic simulations using turbulence fields with the same properties as the measured inflow conditions (IEC, 2015).

To evaluate the lidar-based approaches, we use a virtual lidar simulator that scans the *target* wake fields, and, through ~~a~~ our proposed wake field reconstruction technique, incorporates these samples in a random turbulence ~~seed~~ field realization from *set B* ~~.~~ (see Fig. 1). This numerical approach intends to imitate what we would eventually do when nacelle lidar measurements within wakes are available for load predictions.

Further, by incorporating lidar retrievals in the wind field reconstruction technique, we expect to reduce the amount of statistical uncertainty as the load time series resulting from this approach will have greater similarity with the load time series based on the *target* turbulence fields. Therefore, this procedure allows us to quantify the uncertainty of load predictions that results from lidar-reconstructed wake fields (see the red elements in Fig. 1) against the *target*, and at the same time, to compare the associated statistical uncertainty with that of the *baseline*. To summarize, the following load simulation cases are defined:

- *Target*: ~~DWM-based~~ DWM model-based wake fields imposed on random turbulence ~~seeds~~ field realizations from *set A*.
- *Baseline*: ~~DWM-based~~ DWM model-based wake fields imposed on random turbulence ~~seeds~~ field realizations from *set B*.
- *Constrained simulations (CS)*: lidar-reconstructed wake fields, where lidar virtual measurements of the *target* fields are incorporated as constraints to random turbulence field realizations from *set B*.
- *Wake deficit simulations (WDS)*: lidar-reconstructed wake fields, where lidar virtual measurements of the *target* fields are fitted to a wake deficit shape function to compute wake deficits, which are then superimposed to random turbulence field realizations from *set B*.

The load validation comprises a large number of simulations ~~in order~~ (we use eighteen random turbulence field realizations for each individual 10-min statistic of the inflow wind), to quantify the statistical uncertainty of power and load predictions under ~~a variety of inflow conditions .~~ inflow conditions measured at a site. More details on the load validation analysis are provided in Sect. 4.2. Eventually, we quantify the load uncertainties of the *baseline*, *CS*- and *WDS*-methods by comparison to the loads of the *target* simulations, and we define two main criteria to evaluate the proposed approaches:

I The mean bias of all load predictions obtained with the lidar-reconstructed *CS*- and *WDS*-simulations is ~~of the same order of~~ equal to that obtained with the *baseline*.

II The statistical uncertainty (~~i.e. standard deviation of the bias~~here defined as the standard deviation computed from all biases (Dimitrov and Natarajan, 2017; Conti et al., 2020b)) derived with the lidar-reconstructed *CS*- and *WDS*-simulations is lower than that obtained with the *baseline*.

Provided that these criteria are satisfied, the proposed lidar-based ~~reconstruction approaches~~ wake field reconstruction techniques will produce (I) power and load predictions in wakes ~~, which are in a statistical sense as accurate as~~ that are

statistically unbiased compared to the DWM model results, and (II) a reduced statistical uncertainty in power and load predictions compared to the DWM model results, which is achieved by reconstructing wake fields ~~that have~~ with stronger similarities to the ~~*target* fields compared to the DWM model results~~actual inflow.

3 Methodology

3.1 Mann turbulence spectral model

The time-domain aeroelastic simulations require input of a three-dimensional turbulence field that mimics atmospheric turbulence (Dimitrov et al., 2017). For this purpose, the IEC 61400-1 recommends, i.a., the Mann uniform shear spectral tensor model (Mann, 1994) or the Kaimal model (Kaimal et al., 1972). The turbulence spectral properties of a three-dimensional homogeneous wind field are described by the spectral velocity tensor $\Phi_{ij}(\boldsymbol{k})$ (Kristensen et al., 1989):

$$\Phi_{ij}(\boldsymbol{k}) = \frac{1}{(2\pi)^3} \int R_{ij}(\boldsymbol{r}) \exp(i\mathrm{i}\boldsymbol{k}\cdot\boldsymbol{r}) d\boldsymbol{r}, \tag{1}$$

which is the Fourier transform of the covariance tensor $R_{ij}(\boldsymbol{r})$, $\boldsymbol{r} = (x, y, z)$ is the spatial separation vector defined in a right-handed coordinate system such that the longitudinal component of the wind field (u) is in the x direction, y and z are the directions of the ~~transversal components , and~~ transverse components (i.e., the v- and w-velocity components), and $\boldsymbol{k} = (k_1, k_2, k_3)$ is the ~~wave~~ vector with the wavenumbers in the (x, y, z) directions.

The model by Mann (1994) (hereafter referred to as the Mann model), assumes neutral atmospheric conditions and defines the spectral tensor as function of three input parameters: $\alpha_k \epsilon^{2/3}$, which is a product of the spectral Kolmogorov constant α_k and the turbulent energy dissipation rate ϵ, Γ is a parameter describing the anisotropy of the turbulence, and L is a length scale proportional to the size of turbulence eddies. From the spectral tensor, the cross-spectra between two points located in a y–z plane and separated by a distance (Δ_y, Δ_z) are calculated numerically by:

$$\chi_{ij}(k_1, \Delta_y, \Delta_z) = \int\int \Phi_{ij}(\boldsymbol{k}, \alpha_k \epsilon^{2/3}, L, \Gamma) \exp(ik\mathrm{i}k_2\Delta_y + i\mathrm{i}k_3\Delta_z) dk_2 dk_3. \tag{2}$$

Further, by inverse Fourier-transforming the cross spectrum χ_{ij}, we can derive the auto- and cross-correlation structure of the turbulence field (Dimitrov and Natarajan, 2017), as:

$$R_{ij}(\Delta_x, \Delta_y, \Delta_z) \propto \int \chi_{ij}(k_1, \Delta_y, \Delta_z) \exp(ik\mathrm{i}k_1\Delta_x) dk_1. \tag{3}$$

3.2 Dynamic Wake Meandering model

The DWM model ~~simulates the~~ is an engineering wake model that simulates wind field time series and includes three components: a quasi-steady velocity deficit, the wake-added turbulence, and the wake meandering (Madsen et al., 2010). Figure 2 illustrates these wake features components qualitatively.

The DWM model assumes wakes as passive tracers displaced in the lateral and vertical ~~movements of~~ directions by the large eddies in the atmospheric flow. Further, the quasi-steady wake deficits are advected in the stream-wise direction adopting

Taylor's assumption of frozen turbulence (Madsen et al., 2010). This set of assumptions allows decoupling the wake deficit ~~by superimposing these deficits on a random and homogeneous turbulent wind field ,~~ and wake-added turbulence components from the wake meandering model (Larsen et al., 2007). Hence, the three components of the DWM model are computed separately and subsequently superposed on random homogeneous turbulence field realizations (e.g., ~~that~~ generated using the Mann model~~.~~) to produce three-dimensional wake field time series that are input to aeroelastic simulations (Larsen et al., 2013; Keck et al., 2014) .

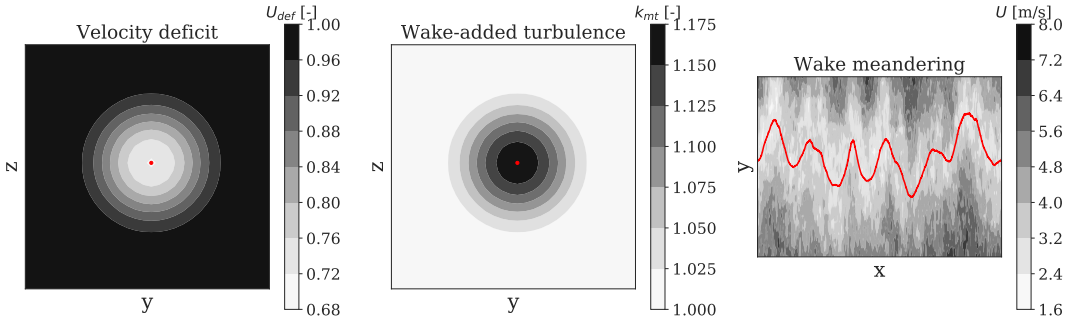

Figure 2. Qualitative representation of the three wake components predicted by the DWM model, including an axisymmetric quasi-steady velocity deficit, which is defined as the local wind speed U divided by the ambient wind speed $\bar{U}_{amb}$ (left), a wake-added turbulence scaling factor, k_{mt} (middle), and the meandering of the quasi-steady wake deficit superposed on a random homogeneous turbulence field realization (right). The red marker identifies the wake center position and the red solid line the wake center's trajectory in the longitudinal x- and lateral y-coordinate. The wake also meanders in the vertical direction (not shown). The wake features are computed for an ambient inflow characterized by $\bar{U}_{amb}$= 6 m/s and a turbulence intensity of TI_{amb}=8%.

The velocity deficit definition is based on the work of Ainslie (1986, 1988), who applied a thin shear-layer approximation of the Navier–Stokes equations and a simple eddy viscosity formulation. The wake deficit ~~development~~ expansion and recovery downstream of the generating turbine is driven by the turbulent mixing occurring due to the ambient turbulence and the turbulence generated by the wake shear field itself ~~(Madsen et al., 2010). The recent work of Keck et al. (2014, 2015) included atmospheric stability effects on the eddy viscosity formulation.~~ (Madsen et al., 2010; Keck et al., 2014, 2015). For a given wind turbine aerodynamic rotor design, a 10-min average inflow wind speed ($\bar{U}_{amb}$), and ambient turbulence intensity (TI_{amb}), the DWM model calculates a two-dimensional quasi-steady velocity deficit defined in the meandering frame of reference (MFoR), which is a coordinate system with origin in the center of symmetry of the deficit, as shown in Fig. 2-left. Here, we use the numerical scheme of the standalone DWM model (Liew et al., 2020; Larsen et al., 2020) to compute the quasi-steady velocity deficit.

The wake-added turbulence ~~that originates~~ originating from the breakdown of tip vortices and from the shear of the velocity deficit is accounted for by a semi-empirical turbulence scaling factor ~~. This factor~~ (Madsen et al., 2010) as:

$$k_{mt}(y,z) = \mid 1 - U_{def}(y,z) \mid k_{m1} + \left| \frac{\partial U_{def}(y,z)}{\partial y \partial z} \right| k_{m2}, \tag{4}$$

where U_{def} is the axisymmetric velocity deficit in the MFoR (see also Fig. 2-left), and k_{m1} and k_{m2} are calibration constants (Madsen et al., 2010). The two-dimensional spatial distribution of k_{mt} is shown in Fig. 2-middle. As wake turbulence is both highly isotropic and characterized by a reduced turbulence length scale compared that of the ambient turbulence (Madsen et al., 2005), k_{mt} of Eq. (4) scales the residual field of a ~~Mann-based turbulence field generated~~ Mann-generated turbulence field assuming isotropic turbulence, i.e., $\Gamma = 0$, and a small turbulence length scale ($L \approx 10$–25% of the ambient turbulence length scale) (Madsen et al., 2010). ~~Both the wake deficit and wake-added turbulence profiles are resolved in the meandering frame of reference, which is a coordinate system with origin in the center of symmetry of the wake deficit. The DWM model considers wakes as passive tracers driven by the large turbulence scales of the inflow. Madsen et al. (2010) defined large turbulent scales as those measuring~~

The wake meandering is assumed to be governed by the atmospheric turbulent structures of the order of two rotor diameters (~~D~~D) or larger ~~, an assumption validated~~ (Madsen et al., 2010). This assumption was verified using lidar observations of ~~wake fields (Bingöl et al., 2010; Trujillo et al., 2011). The wake is advected downstream with~~ wakes (Bingöl et al., 2010; Trujillo et al., 2011). Thus, the simulated wake meandering time series is obtained by low-pass filtering atmospheric turbulence fluctuations (i.e., v- and w-velocity components measured from a local mast or lidar, or alternatively simulated by the Mann model) by a cut-off frequency $f_{cut\text{-}off} = \bar{U}_{amb}/(2D)$, which excludes contributions from smaller eddies to the meandering dynamics (Larsen et al., 2008).

As a result, the wake field simulated by the DWM model can be seen as a 'cascade' of quasi-steady velocity deficits that meander in the lateral and vertical directions and are advected downstream by the mean wind speed ~~using Taylor's frozen turbulence hypothesis. Recent studies have calibrated and validated the DWM-predicted wake deficits against high-fidelity wake field simulations (Keck et al., 2014, 2015), wind turbine operational data (Larsen et al., 2013) and only recently, lidar measurements of~~ of the inflow using Taylor's assumption. These wake features are superposed on stochastic homogeneous turbulence field realizations to generate wake fields time-series that are then input to aeroelastic simulations (see Fig. 2-right).

Mathematically, a three-dimensional synthetic wake flow field compliant with the DWM model formulation can be defined by a linear superposition of the ambient wind field and two inhomogeneous turbulence terms as:

$$U_{\mathrm{DWM}}(x,y,z) = \bar{U}_{amb}(z) + u'_{i,K_{def}}(x,y,z) + u'_{j,K_{turb}}(x,y,z), \tag{5}$$

where $\bar{U}_{amb}(z)$ is the ambient wind speed including the atmospheric vertical wind shear profile, $u'_{iK_{def}}(x,y,z)$ is a residual turbulence field with imposed wake deficits that follow the meandering path, and $u'_{j,K_{turb}}$ is a second turbulence field modelling wake-added turbulence effects. Adopting Taylor's assumption, the wake field ~~(Reinwardt et al., 2020). Figure 2 shows the wake deficit (K_{def}) and wake-added turbulence profiles (K_{mt}) derived from the DWM model and the DTU~~ can be described by the

spatial vector solely; thus, the time variable is disregarded in Eq. (5). The subscripts i, j indicate two random and uncorrelated turbulence field realizations. The $u'_{i,K_{def}}$ field is computed as:

$$u'_{i,K_{def}}(x,y,z) = \bar{U}_{amb}(z)K_{def}(x,y,z) + u'_i(x,y,z) - \bar{U}_{amb}(z), \quad (6)$$

where $K_{def}(x,y,z)$ denotes the DWM model-based wake deficit time-series including a pre-computed stochastic meandering path, and u'_i is a random homogeneous turbulence field realization from the Mann model with the same Mann parameters as those of the ambient wind field. Note that $K_{def}(x,y,z)$ assumes values equal to unity when wake losses are not present. The Mann parameters, $\alpha_b \epsilon^{2/3}$, L, and Γ, are derived, e.g., from fitting the free-stream observed turbulence velocity spectra with the Mann model with the use of pre-computed look-up-tables (Peña et al., 2017). The wind field formulation of Eqs. (5) and (6) is consistent with the domain of wind fields typically input to aeroelastic simulations (Larsen and Hansen, 2007). Finally, $u'_{j,K_{turb}}$ is obtained as:

$$u'_{j,K_{turb}}(x,y,z) = u'_j(x,y,z)K_{mt}(x,y,z), \quad (7)$$

where $K_{mt}(x,y,z)$ denotes a time-series of turbulence's scaling factors computed from Eq. (4) including a pre-computed stochastic meandering path, u'_j is a random homogeneous turbulence field with Γ=0 and L= 10~~MW wind turbine, as function of ambient wind speed and turbulence.As illustrated, the depth of the wake deficit decreases for increasing inflow wind speed and turbulence , due to the reduced rotor thrust coefficient and the enhanced turbulence mixing. The wake-added turbulence is proportional to the depth and gradient of the velocity deficit profile; thus a faster recovery of the deficit induces lower added turbulence . Steady wake characteristics predicted by the DWM model at the downstream distance of 5 D, D being the rotor diameter, resolved in the radial direction and normalized on the rotor radius (R = 89.5 m). Left and middle: wake deficit profiles as function of ambient wind speed and ambient turbulence. Right: wake-added turbulence profiles as function of the ambient turbulence.~~ % of the ambient turbulence length scale (Madsen et al., 2010).

3.3 Lidar simulator

We use the lidar simulator developed within the ViConDAR ~~open source~~ open-source numerical framework to virtually replicate lidar measurements (https://github.com/SWE-UniStuttgart/ViConDAR), (Pettas et al., 2020). The lidar simulator derives the line-of-sight (LOS) velocities at each scanning location ~~,~~ by transforming the u-, v- and w-velocity components of the synthetic turbulence field into a LOS coordinate system. To simulate the probe volume of the lidars, a Gaussian weighting function $W(F,r)$ is imposed along the LOS coordinate r and centered at the focal distance F:

$$V_{LOS,eq} = \int V_{LOS}(r)W(F,r)dr. \quad (8)$$

The u-velocity is computed from the projection of $V_{LOS,eq}$ onto the longitudinal axis, i.e., the v- and w-velocity components are neglected in the field reconstruction ~~(Schlipf et al., 2013; Simley et al., 2013; Pettas et al., 2020). The latter increases the uncertainty of the procedure.~~ (Schlipf et al., 2013; Simley et al., 2013). This assumption leads to:

$$u_{lidar} = \frac{V_{LOS,eq}}{\cos\phi\cos\theta}, \quad (9)$$

where ϕ is the elevation and θ the azimuth angle of the scanning pattern (Peña et al., 2017). Neglecting the v- and w-velocity components introduces uncertainty in the wind field reconstruction. However, the opening angles (ϕ, θ) relative to the scanning configurations of our work reach a maximum of 35° (see Sect. 3.3.1); thus, the introduced errors by Eq. (9) are marginal (Simley et al., 2013).

Other sources of uncertainty ~~inherent to the use of~~ in the radial velocity estimation inherent to lidars, e.g., from the optics and internal signal processing, are accounted for by adding a Gaussian white noise. Here we add noise at a level that results in a signal-to-noise ratio of -20 dB ~~, as shown~~ as in Pettas et al. (2020). We do not investigate the sensitivity of the noise level in the present work.

The lidar simulator can mimic any arbitrary scanning pattern and includes a time-lag between each lidar-sampled ~~measurements~~ measurement to resemble the scanning frequency (see Fig. 3). In the present study, the virtual lidar data are computed from the synthetic wake flow fields generated using the DWM model. These wind fields are time series of the u-, v- and w-velocity components defined over a turbulence box with a grid size of 8192×32×32 ~~(x, y, z)~~ $(x \times y \times z)$. A spatial resolution of 6.5 m is used for the grid in the rotor plane, which leads to a turbulence box with dimension 208 m × 208 m in both lateral and vertical directions ~~(y, z), while the spatial resolution in the longitudinal axis~~ $(y \times z)$. The spatial resolution dx in the x-axis depends on the simulated ~~wind speed~~ambient wind speed at hub height, $dx = (\bar{U}_{amb} T_{sim})/8192$, where T_{sim} is the simulation time in seconds. These dimensions ensure an adequate turbulence field for a ~~10 min~~ 10-min wind field simulation over a large rotor ~~,~~and a space-time resolution such that the probe volume effects can be captured by the virtual lidar ~~.~~ (Dimitrov et al., 2017; Pettas et al., 2020).

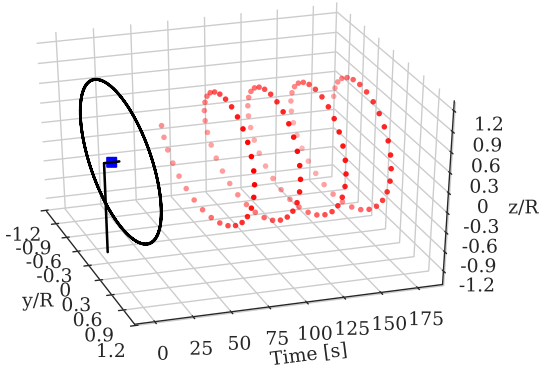

Figure 3. An illustration of the virtual lidar simulator setup run for 175 s with simulated time lag. The wind turbine is sketched by the black solid lines, the nacelle-mounted lidar is represented by a blue squared marker measuring upfront the turbine. The trajectory of the scanning beam is shown by discrete red dots.

3.3.1 Lidar scanning strategies

Several nacelle-mounted lidars have been developed both for commercial and research purposes. These include continuous-wake (CW) and pulsed lidar (PL) technologies. The CW and PL lidars differ in the emission waveform, and in the temporal and spatial resolution, among others (Peña et al., 2015). The Windar Photonics 2- and 4-beam CW lidars have been applied for wake detection purposes (Held and Mann, 2019a) and rotor-effective wind speed estimation (Held and Mann, 2019b). The ZephIR Dual Mode (DM) circular-scanning CW lidar, with a single beam and sampling frequency of approximately 50 Hz, has been used for several purposes including power curve assessment (Medley et al., 2014), wind field reconstruction (Borraccino et al., 2017), turbulence characterization (Peña et al., 2017), and load validation in both free and wake conditions (Dimitrov et al., 2019; Conti et al., 2020a). Based on the ZephIR, a research lidar, the SpinnerLidar (SL), was developed (Peña et al., 2019). The SL uses two rotating prisms that scan the inflow at 400 points in 1–2 s. Due to the scanning pattern, the SL can be used for detailed wake characterization (Herges and Keyantuo, 2019; Doubrawa et al., 2019). A five-beam PL lidar developed by Avent Lidar Technology was used in several experiments (Bos et al., 2016; Borraccino et al., 2017). This lidar does not longer exist, but a 4-beam version by Leosphere is on the market. The lidar developed by the Stuttgart Wind Energy (SWE) group builds on the commercial Windcube WLS-7 from Leosphere and is adapted with a scanner device with two degrees of freedom for nacelle installation in order to scan the wind field in any direction. Currently, the SWE lidar scans at five ranges with a maximum of 49 points per range in approximately 8.4 s (Rettenmeier et al., 2014).

The recent work of Pettas et al. (2020), who combined a lidar simulator and a field reconstruction approach, showed that a 7-beam lidar can potentially increase the accuracy of reconstructed wind fields. For wake characterization, Doubrawa et al. (2016) indicated that the coverage of the scanning geometry is the key to adequately track the wake center location in time, and the scanning density to accurately estimate the velocity deficit distribution within the wake.

To evaluate the ability of To evaluate currently available lidars' ability to perform wake characterization, we select a few standard scanning configurations and use them to perform load validation within wakes. These are a 4-beam lidar (4P) (Held and Mann, 2019a, b), an extended configuration with 7 beams, six arranged at the corner of a hexagon and a central beam (7P) (Pettas et al., 2020), the conical scanning lidar (Cone) (Medley et al., 2014; Borraccino et al., 2017; Peña et al., 2017), the SpinnerLidar (SL) (Peña et al., 2019; Herges and Keyantuo, 2019; Doubrawa et al., 2019), the SL, and a general grid pattern (Grid) covering the full turbulence box (see Fig. 4).

The 4P and 7P patterns mimic measurements from a PL lidar obtained with a single scanning beam pointing at a fixed location, whereas the Cone, the SL and the Grid configurations mimic those from a CW lidar. Thus, a

A time lag between each sampling beam is simulated, and all the patterns are assumed to measure at the same single range. Although we do not optimize the scanning patterns, we use scan radii of (defined as the radius between hub height and the location of the scanned points) of about 70–80% of the rotor radius to estimate wind field characteristics based on previous recommendations (Dimitrov and Natarajan, 2017; Simley et al., 2018). Thus, we define the 4P, 7P, and Cone patterns accordingly . as shown in Fig. 4. The SL trajectory is scaled to cover the full rotor areaand the Grid pattern has a spatial

~~resolution of~~ , and the positions over the plane of measurement are separated by 29 m ~~.~~ in both vertical and transverse directions for the Grid pattern.

A preview distance of 0.7D is assumed. Note that increasing the preview distance reduces the errors caused by the cross-contamination effects of the ~~v and w components~~v- and w-components and reduces the induction effects, but raises errors due to the wind evolution (Simley et al., 2012). ~~More technical details on the scans are provided in Table 1.~~ These effects are not investigated in detail in this work, as we use DWM model-based wake fields as *target*, which do not include induction effects nor turbulence evolution as the Taylor's assumption is applied.

We assume a 2-s scan-period for all the simulated configurations, which refers to the time required for a beam to complete the full pattern. Given the finite resolution of the synthetic turbulence boxes (i.e., 6.5 m in both lateral and vertical directions), the Cone and SL scanned locations are binned within the box grid, as reported in Table 1.

A probe volume with an extension of 30 m in the LOS direction is assumed for all the analyzed patterns ~~. We~~ (Peña et al., 2015) . Here, we define the probe volume's length as the standard deviation of the Gaussian weighting function for convenience. Alternatively, the weighting function can be defined by a Lorentzian form (Mann et al., 2010); however, the differences in the reconstructed wind velocity arising from a Gaussian- or Lorentzian-like weighting function are marginal (Dimitrov et al., 2019) . Further, we also define an additional case (Grid*) that neglects probe volume averaging effects (see Table 1).

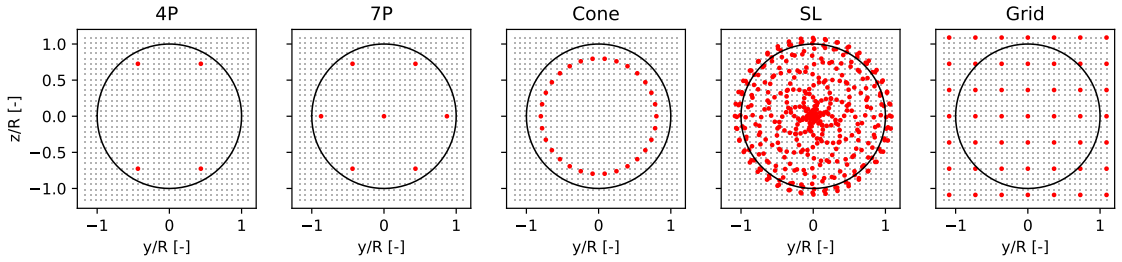

Figure 4. Selected lidar scanning patterns for the load analysis. The red markers indicate the scanned locations and the black dots in the background define the spatial resolution of the turbulence box. The rotor diameter is shown in a black solid line.

3.4 Wake field reconstruction techniques

~~A three-dimensional synthetic wake flow field, compliant with the DWM formulation, can be defined by a linear superposition of the ambient wind field and two turbulence terms as:~~

$$U_{wake}(x,y,z) = \bar{U}_{amb}(z) + u'_{i,K_{def}}(x,y,z) + u'_{j,K_{turb}}(x,y,z),$$

Table 1. Technical properties of the simulated lidar scanning configurations. Note that the Cone and SL measurements are binned according to the spatial resolution of the synthetic turbulence fields, thus leading to a reduction of the simulated scanning positions.

Scanning configuration	Measurements / scan (binned) [-]	Sampling frequency [Hz]	Scan period [s]	Measurements / 10-min [-]	Probe volume size [m]
4P	4	2	2	1200	30
7P	7	3.5	2	2100	30
Cone	100 (30)	50	2	9000	30
SpinneLidar (SL)	400 (93)	200	2	27900	30
Grid	49	25	2	14700	30
Grid*	49	25	2	14700	0

where $\bar{U}_{amb}(z)$ is the ambient wind speed including the atmospheric wind profile, $u'_{iK_{def}}(x,y,z)$ is a residual turbulence field with imposed wake deficits, and $u'_{j,K_{turb}}$ is a second turbulence field modelling wake-added turbulence effects. The subscripts i,j indicate two random field realizations. The $u'_{i,K_{def}}$ field can be computed as:

$$u'_{i,K_{def}}(x,y,z) = \bar{U}_{amb}(z)K_{def}(x,y,z) + u'_i(x,y,z) - \bar{U}_{amb}(z),$$

where K_{def} is the radial symmetric wake deficit time-series including a pre-computed stochastic meandering process calculated with the DWM model, and u'_i is a random turbulence realization from the Mann model with spectral properties as for the ambient wind field. The spectral properties of the turbulence are defined by $\alpha_k\epsilon^{2/3}, L, \Gamma$, which can be fitted based on freestream observations. The wind field formulation of Eqs. and is consistent with the domain of wind fields typically input to aeroelastic simulations. Finally, $u'_{j,K_{turb}}$ is obtained by simply scaling an isotropic turbulence field with low turbulence length scales, by the semi-empirical formulation in Eq. (19) in Madsen et al. (2010). By defining the *target* DWM model-based wake flow fields with the DWM formulationas the *target* fields, the underlying assumptions on which we define the wind lidar-based wake field reconstruction techniques are:

1. The ambient wind conditions are known, including $\bar{U}_{amb}(z)$, the atmospheric turbulence intensity (TI_{amb}), and the atmospheric stability conditions (here implicitly prescribed through the Mann parameters: $\alpha_k\epsilon^{2/3}, L, \Gamma$).

2. The lidar-based wake fields can be are reconstructed by incorporating lidar observations (e.g., in the form of constraints or lidar-fitted velocity deficits) into a zero-mean, homogeneous, and random Gaussian turbulence field generated by the Mann spectral tensor model.

3. The induction effects on lidar measurements are neglected and the Taylor's frozen turbulence hypothesis is assumed.

4. The Only the u-velocity fluctuations are recovered from the *target* reconstructed from the *target* wake fields.

The corresponding random turbulence seeds field realizations from *set A* and *set B* have similar spectral properties, ; however, these fields only describe the turbulence structures in the freestream conditionsof the ambient wind field. The lidar measure-

ments of the wake field, combined with the wake field reconstruction approach, should recover the whole information regarding the wake characteristics, including velocity deficits, wake-added turbulence, and meandering in lateral and vertical directions. Further, the first assumption is ~~not~~ no longer needed if a second instrument is deployed at the site measuring the ~~freestream conditions(Borraccino et al., 2017; Peña et al., 2017).~~ ambient conditions, for example, using a mast or a nacelle-mounted lidar (Borraccino et al., 2017; Peña et al., 2017).

The second and third assumptions are inherent in the modelling approach and limitations of the DWM model ~~, as well as~~ and other analytical wake models; however, in this study, the wake characteristics are extracted directly from the lidar observations rather than a physical-based deficit formulation. Eventually, wind turbine responses are mainly affected by the mean wind speed in the longitudinal direction (u-velocity) and its variance (Dimitrov et al., 2018), while the effects of the v- and w-turbulence are generally marginal (Dimitrov and Natarajan, 2017).

3.4.1 Constrained Gaussian field simulations~~(CS)~~

The algorithm for applying constraints on a zero-mean, homogeneous, and isotropic Gaussian random field was developed in ~~Dimitrov and Natarajan (2017). It~~ Hoffman and Ribak (1991), and extended to Mann-generated turbulence fields for aeroelastic simulations in Nielsen et al. (2003) and Dimitrov and Natarajan (2017). The algorithm uses a set of constraints that are ~~here-derived~~ here derived from a virtual lidar simulator and an unconstrained random turbulence realization generated with the Mann spectral tensor model.

Following the notation in Dimitrov and Natarajan (2017), we denote $\tilde{g}(\boldsymbol{r})$, where $\boldsymbol{r} = (x, y, z)$ is the spatial separation vector, an unconstrained random turbulence realization. The spectral property of $\tilde{g}(\boldsymbol{r})$ at each discrete lateral and vertical separation of the turbulence box can be computed from the Mann model in Eq. (2), given a set of parameters $(\alpha_k \epsilon^{2/3}, L, \Gamma)$. We denote a set of constraints as $\boldsymbol{H} = \{h_i(\boldsymbol{r}) = c_i, i, ..., M\}$, where each constraint is a measured time series for a particular spatial location $\boldsymbol{r}$ and M is the total number of constraints. Note that the constraints are defined as a residual wind field; thus, we remove the mean ambient wind speeds from the lidar measurements of Eq. (9), i.e., $c_i = u_{lidar} - \bar{U}_{amb}$, which are the values that are input to the algorithm.

The objective of the algorithm is to define a turbulence field $g(\boldsymbol{r})$, subjected to the constraints in $\boldsymbol{H}$ that maintains the covariance and coherence properties of the unconstrained field $\tilde{g}(\boldsymbol{r})$. As demonstrated in Dimitrov and Natarajan (2017), the unknown points of the field can be defined by maximizing their conditional probability distribution on the constraint set $\boldsymbol{H}$. Thus, we define the residual field $\xi(\boldsymbol{r}) = g(\boldsymbol{r}) - \tilde{g}(\boldsymbol{r})$, which is the difference between the constrained and unconstrained fields. This residual field is also a random Gaussian field, where its values at the constraint locations are known $\xi(\boldsymbol{r_i}) = c_i - \tilde{g}(\boldsymbol{r})$. The values of the residual field at unknown locations can be derived as:

$$\bar{\xi}(\boldsymbol{r}) = \langle \xi(\boldsymbol{r}) | \boldsymbol{H} \rangle = \boldsymbol{\zeta}(\boldsymbol{r}) \boldsymbol{Z}^{-1} (\boldsymbol{H} - \tilde{g}(\boldsymbol{r})), \tag{10}$$

where $\langle . \rangle$ denotes ensemble averaging, $\boldsymbol{\zeta}(\boldsymbol{r})$ is a vector of cross-correlations between the constraints and the field, and $\boldsymbol{Z}$ is the symmetric correlation matrix of the constraints set. Both $\boldsymbol{\zeta}(\boldsymbol{r})$ and $\boldsymbol{Z}$ can be computed from Eq. (3). Eventually, any

constrained realization can be written as a sum of the unconstrained field and the mean of the residual field as:

$$g(\boldsymbol{r}) = \tilde{g}(\boldsymbol{r}) + \boldsymbol{\zeta}(\boldsymbol{r}) Z^{-1}(\boldsymbol{H} - \tilde{g}_r(\boldsymbol{r})). \tag{11}$$

By denoting $u'_{\mathrm{CS,B,i}} = g(\boldsymbol{r})$, as the constrained turbulence field that incorporates lidar measurements into a random turbulence realization i from *set B* (see Fig. 1), we can derive the reconstructed wake flow field to be input in aeroelastic simulations as:

$$U_{\mathrm{CS}}(x,y,z) = \bar{U}_{amb}(z) + u'_{\mathrm{CS,B,i}}(x,y,z). \tag{12}$$

Note that the accuracy of the ~~resulting~~ reconstructed wind field will depend on the fidelity and accuracy of the nacelle lidar measurements used to characterize the wake ~~deficit~~field.

3.4.2 Wake deficit superposition simulations~~(WDS)~~

The wake deficit superposition ~~approach (*WDS*)~~ (*WDS*) approach assumes that velocity deficits can be described by a bivariate Gaussian shape function, which is fitted based on lidar measurements of the ~~*target*~~ *target* wake flow field. Several studies have demonstrated the viability and robustness of the Gaussian curve fitting to track wake deficit displacements in the far-wake region (Trujillo et al., 2011; Reinwardt et al., 2020).

In our study, the wake shape function not only tracks the wake meandering, but it is used to quantify the depth and width of the wake at each quasi-instantaneous scan performed by the lidar. ~~Thus, following the notation~~ Traditionally, the normalized velocity deficit is defined as the difference between the ambient wind speed and that inside the wake as:

$$U_{def}(x,y,z) = \frac{\bar{U}_{amb}(z) - u_{lidar}(x,y,z)}{\bar{U}_{amb}(z)}, \tag{13}$$

where $\bar{U}_{amb}(z)$ is assumed to be known and the lidar measurements in the wake (u_{lidar}) are sampled by the lidar simulator using Eq. (9). Following the procedure of Trujillo et al. (2011), ~~we define the lidar-estimated 'instantaneous' wake deficit $K_{def,lidar}$ as:~~ a bivariate Gaussian shape is used to describe the velocity deficit flow field as:

$$K_{\underline{def,lidar}\,def,Gau}(\underline{x},y,z) = \frac{U_{amb}(z) - U_{lidar}(x,y,z)}{U_{amb}(z)} = \frac{A}{2\pi\sigma_{wy}\sigma_{wz}} \exp\left[-\frac{1}{2}\left(\frac{(y_i-\mu_y)^2}{\sigma_{wy}^2} + \frac{(z_i-\mu_z)^2}{\sigma_{wz}^2}\right)\right], \tag{14}$$

where (μ_y, μ_z) define the wake center location, $(\sigma_{wy}, \sigma_{wz})$ are width parameters of the wake profile in the y and z directions, respectively, (y_i, z_i) denote the spatial location of the LOS and A is a scaling parameter dictating the depth of the wake. ~~As discussed above, we assume that U_{amb} is known, while the lidar measurements in the wake (U_{lidar}) are sampled by the lidar simulator.~~ A least squares method is applied to fit the measured wind speed deficits from Eq. (13) to the bivariate Gaussian function in Eq. (14).

The optimal wake ~~parameters are obtained from a least-squares fitting procedure, which is performed~~ deficit parameters $(\mu_y, \mu_z, \sigma_{wy}, \sigma_{wz}, A)$ are obtained for each completed scanning period (i.e., $\sim$ 2 s as described in Table 1), resulting in

approximately 300 lidar-reconstructed deficits within a 10-min period. Finally, ~~the~~ these lidar-fitted wake deficits are superimposed on a random homogeneous turbulence field realization from *set B*~~.~~, as shown in Fig. 1.

A preliminary analysis ~~shows~~ showed that wide turbulence boxes (208 m $\times$ 208 m) can present large turbulence structures within, i.e., broad regions across the box characterized by low wind speeds, whose sizes can alter the depth and width properties of the lidar-fitted wake deficits in Eq. (14). ~~It follows that~~ As a result, the wake properties of the reconstructed field can considerably deviate from the actual imposed wake characteristics.

To compensate for these deviations ~~, we fit a second Gaussian shape function ($K_{def,\mathrm{WDS}}$) as that from Eq. , which accounts for the turbulence structures within the random turbulence box from *set B*, by reformulating the deficits as:~~

$$K_{def,lidar}(x,y,z) = \frac{U_{amb}(z) - U_{WDS}(x,y,z)}{U_{amb}(z)} = \frac{U_{amb} - (U_{amb}(z)K_{def,\mathrm{WDS}}(x,y,z) + u'_{B,i}(x,y,z))}{U_{amb}(z)},$$

~~where U_{WDS} is the WDS-reconstructed wake field, which~~ and considering that the DWM model-based wake fields can be defined as a linear summation of the ambient wind field ~~U_{amb}~~ $\bar{U}_{amb}$ scaled by the ~~fitted wake function $K_{def,WDS}$, and the random turbulence realization $u'_{B,i}$. This formulation is consistent with that of the DWM model in Eq. .~~ wake deficit function K_{def}, and a random homogeneous turbulence realization term u'_i, as reported in Eq. (6), we reformulate the least squares minimization problem as:

$$\Gamma_{def} = \sum_{mn} \left[U_{def}(y_m, z_n) - \frac{\bar{U}_{amb} - (\bar{U}_{amb}(z)(1 - K_{def,Gau}(y_m, z_n|\mu_y, \mu_z, \sigma_{wy}, \sigma_{wz}, A)) + u'_{B,i}(y,z))}{\bar{U}_{amb}(z)} \right]^2, \quad (15)$$

where subscripts (m,n) indicate data points within the scanning configuration, the second term in the right-hand side defines the velocity deficit as in Eq. (13), in which the reconstructed wake field is defined as $\bar{U}_{amb}(1 - K_{def,Gau}) + u'_{B,i}$ and $u'_{B,i}$ is the random homogeneous turbulence realization from *set B*. Note that when wake losses are present, $(1 - K_{def,Gau})$ will reduce the ambient wind speed, as expected. As the sampling frequency of the lidar is lower than the sampling frequency of the synthetic wind field, we interpolate the fitted wake characteristics at each scan to the whole turbulence field by applying a nearest-neighbor interpolation scheme. Finally, the reconstructed wake field input to aeroelastic simulations is defined by:

$$U_{\mathrm{WDS}}(x,y,z) = \bar{U}_{amb}(z)(1 - K_{def,\mathrm{WDS}}{}_{def,Gau}(x,y,z)) + u'_{B,i}(x,y,z), \quad (16)$$

where $K_{def,Gau}(x,y,z)$ is fitted using Eq. (15) for each completed scan by the nacelle lidar.

4 Results

The results are ~~presented in three main parts. Firstly~~divided into three parts. First, we assess the accuracy of lidar-reconstructed wake fields against ~~*target*~~ *target* fields in Sect. 4.1. ~~Secondly~~Second, we carry out the load validation analysis in Sect. 4.2, and separately present the load ~~predictions uncertainty relative to the *CS*~~prediction uncertainty of the *CS*-approach in Sect. 4.2.2 and that of the ~~*WDS*~~*WDS*-approach in Sect. 4.2.3. A ~~more~~ detailed analysis of the predicted load time-series and load spectral properties is conducted in Sects. 4.2.4 and 4.2.5. Finally, we evaluate the sensitivities of both atmospheric turbulence conditions ~~as well as~~ and the selected lidar technical specifications on the load ~~predictions~~ prediction accuracy in Sect. 4.3.

4.1 Uncertainty of reconstructed wake fields

In this section, we evaluate the accuracy of the lidar-reconstructed fields against ~~*target*~~ the *target* fields. At first, we assess the accuracy of the reconstructed u-velocity ~~component~~ time-series across the turbulence box, by computing the root mean square error, ~~RMSE $= \sqrt{1/n \sum_i^n (\tilde{y}_i - \hat{y}_i)^2}$~~ RMSE $= \sqrt{1/n \sum_i^n (\tilde{y}_i - \hat{y}_i)^2 / \bar{y}_i}$, between the ~~reconstructed~~ lidar-reconstructed ($\tilde{y}$) and ~~*target*~~ *target* velocity ($\hat{y}$), where n = 8192 is the grid size of the box in the ~~time~~ longitudinal direction, normalized over the mean ~~*target* velocity~~ *target* velocity ($\bar{y}_i$) at each grid point of the turbulence box. ~~Then, we derive a measure of the 'explained' variance by the lidar measurements. The explained variance ratio (ρ_E^2) is defined in Dimitrov and Natarajan (2017) as~~ The normalized RMSE indicates if the lidar-reconstructed fields are unbiased compared to the *target* fields (see Fig. 5-top row).

Further, we compute the explained variance ratio across the turbulence box $\rho_E^2 = (\mathrm{cov}(\tilde{y}, \hat{y}) / \sigma_{\tilde{y}} \sigma_{\hat{y}})^2$ (i.e., the square of the Pearson's correlation coefficient (Achen, 1982)), which defines the proportion of the variance in the ~~actually measured~~ inflow field that is transferred to the unconstrained turbulence field by imposing the constraints ~~. This is computed as the square of the cross-correlation coefficient $\rho_E^2 = (\mathrm{cov}(\tilde{y}, \hat{y}) / \sigma_{\tilde{y}} \sigma_{\hat{y}})^2$, between reconstructed ($\tilde{y}$) and *target* ($\hat{y}$) wind speed fluctuations at each grid point. As the *target* and reconstructed~~ (Dimitrov and Natarajan, 2017). As the *target* and lidar-reconstructed fields are based on two sets of random uncorrelated turbulence ~~seeds~~field realizations (see *sets A* and *B* in Fig. 1), $\rho_E^2 \sim 0$ is expected across the box, if no lidar information was included. Contrarily, $\rho_E^2 = 1$ indicates that the reconstructed time-series is fully-correlated with the ~~*target*~~*target*, thus the ~~variance of the reconstructed field matches that of the *target* field~~two fields match completely.

Figure 5 also shows the spatial distribution of ~~the normalized RMSE and~~ ρ_E^2 derived from the ~~*CS*~~*CS*- and ~~*WDS*~~*WDS*-reconstructed fields, with the 7P, Cone, and Grid configurations (see Table 1 for specifications). For this particular analysis, the ~~simulations are run at the downstream distance of 5 D~~turbine of interest is located 5D downstream of the upstream turbine, where D = 179 m is the diameter of the DTU 10 MW turbine, and ambient conditions characterized by U_{amb} = 6 m/s ~~,~~ and TI_{amb} = 8 %. The ~~atmospheric vertical~~ inflow wind profile is defined by a ~~power law model with~~ power-law model with a shear exponent of 0.2. ~~It can be seen that~~

As shown in Fig. 5, the locations of the imposed constraints are characterized by the lowest RMSE and highest ρ_E^2. This effect is more pronounced for the ~~*CS*~~ *CS* results, as the algorithm imposes the actual observations directly in the synthetic field. The RMSE would tend to zero, if the length of probe volume is neglected, the lidar's sampling frequency corresponds to the sampling frequency of the wind field, and cross-contamination effects are compensated. ~~It can also be observed that the~~ The RMSE increases (and ρ_E^2 decreases) for spatial regions that are farther from the lidar's beams. This occurs due to the covariance structure of the unconstrained turbulence field, for which the unknown points are nearly uncorrelated with the imposed constraints.

The errors introduced by the ~~*WDS*~~*WDS*-fields are partly a consequence of an ~~erroneous~~ inaccurate estimation of the wake deficit ~~parameters~~ characteristics (i.e., due to the limited spatial scanning configuration) ~~, and due to~~ and the small-scale turbulence structures contained in the turbulence box. Finally, the results ~~of~~ in Fig. 5 ~~confirms that the spatial resolution of the scanning patterns~~ confirm that the amount of scanned positions by the lidar has a significant impact on the ~~accuracy~~

reconstructed fields' accuracy affecting both the mean and variance of the reconstructed ~~fields~~u-velocity component. Therefore, patterns that cover a larger region of the rotor ~~can~~ lead to more accurate field representations (Dimitrov and Natarajan, 2017; Pettas et al., 2020).

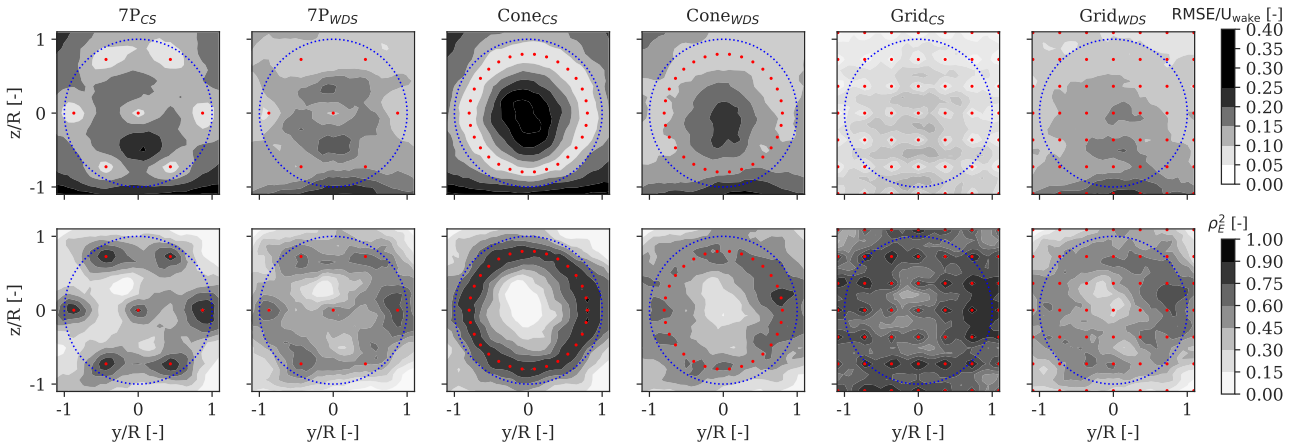

Figure 5. ~~Error visualization~~ Spatial distribution of the ~~*CS*~~error inherent to the *CS*- and ~~*WDS*~~*WDS*-reconstructed fields for selected scanning configurations. The top row refers to the RMSE normalized over the $target$ velocity at each grid point. The bottom row refers to the explained variance ratio. The red markers identify the centers of the lidar beam sampling volumes. The wind turbine rotor is shown in blue.

In Fig. 6, we ~~show a comparison of~~ compare the lidar-reconstructed u-velocity time-series extracted at hub height, using the Grid pattern, with the ~~*target*~~ *target* observations derived at the same location. The ~~*target*~~ *target* wake field is simulated with U_{amb} = 6 m/s and TI$_{amb}$ = 8%. The time-series of the virtual lidar measurements is also shown. ~~It is seen~~ We find that both field reconstruction approaches can predict the reduced wind speed ~~observed in~~ within the wake region ~~as well as recover in details~~ and recover the details of the wind speed fluctuations of the ~~*target*~~ *target* field. However, uncertainty is introduced due to the limited lidar sampling frequency, the ~~length of the probe volume~~ probe volume length (here assumed ~~of~~ to be 30 m)~~and by~~, and the adopted field reconstructing ~~approaches~~techniques. The results ~~of~~ in Fig. 6 demonstrate that incorporating lidar data directly in the reconstructed field (i.e.~~*CS*~~, the *CS*-approach) leads to reproducing more accurate fields compared to the ~~*WDS*~~*WDS*-approach.

In addition, we compute the power spectral density (PSD) of the above analyzed time series of u-velocity fluctuations for a 10-min simulation ~~, and compare the results~~ and compare them in Fig. 7. We observe that the PSD of the reconstructed fields is comparable to that of the ~~*target*~~ *target* for frequencies up to $\approx$ 1 Hz, while the energy spectral content at higher frequencies is ~~considerably~~ attenuated. According to ~~the definition in~~ Larsen et al. (2008), the dominant frequency of the wake meandering is defined as ~~$f_{cut,off} = U/(2D)$, which results in 0.016~~ $f_{cut,off} = U_{amb}/(2D) = 0.016$ Hz ($\sim$ 62 s period) for $U_{amb} = 6$ m/s. As the lidar completes a full-scan in ~~about~~ 2 s, the large-scale wake meandering dynamics are well-captured. Further, as the

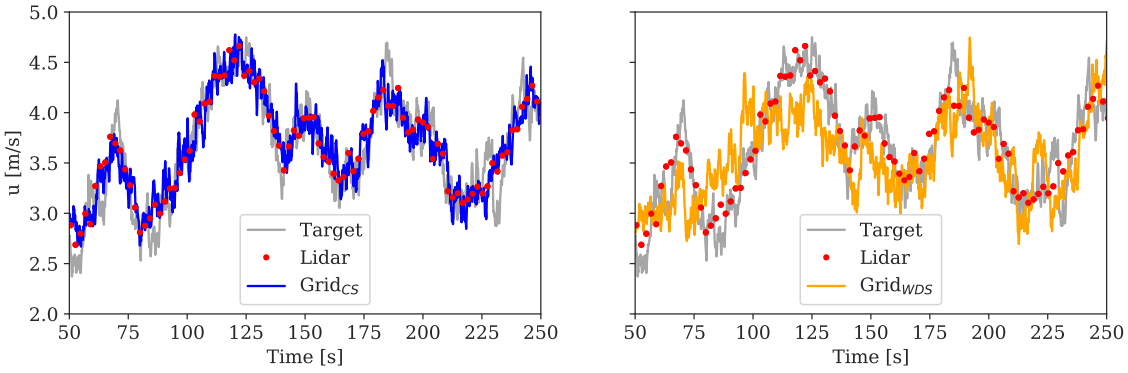

Figure 6. Comparison between the ~~*target*~~ *target* u-velocity time-series at hub height (grey solid line) and the reconstructed field based on the ~~*CS*~~*CS*-approach (left) and ~~*WDS*~~ *WDS* (right) extracted at hub height. The lidar data are shown in red. The ~~*target*~~ *target* simulations are run with U_{amb} = 6 m/s and TI_{amb} = 8%.

wake meandering is the main source of wake added turbulence (i.e., u-component variance), the energy spectral content in the ~~low frequency~~ low-frequency range is recovered~~.~~, as shown in Fig. 7.

The enhanced turbulent energy content ~~in the~~ of the *target* field within the high-frequency range (> 1 Hz) ~~, observed in the *target* field,~~ originates from the small-scale wake added turbulence (Madsen et al., 2010; Chamorro et al., 2012). These effects are not fully recovered in the reconstructed fields, mainly due to the lidar probe volume and limited sampling frequency. ~~Nevertheless, the contribution of these sources of uncertainty on the power and load prediction accuracy is the subject of this study.~~

4.2 Load validation

The DTU 10 MW reference wind turbine is used for the load validation analysis (Bak et al., 2013). The load simulations are carried out using the aeroelastic code HAWC2 ~~(Larsen et al., 2007)~~ (Larsen and Hansen, 2007) and inflow wind conditions measured from an offshore site, as described in ~~the next section (~~Sect. 4.2.1~~)~~. Note that we run the analysis based on offshore wind conditions, which are characterized by low turbulence~~, thus~~; thus, wake effects are more prominent.

This work evaluates the load prediction accuracy at the main wind turbine structures, such as blades, shaft, and tower. Therefore, we neglect the modelling of the offshore substructures and foundations, and we use the onshore model of the DTU 10 MW.

Following the load validation procedure ~~described in Sect. 2~~illustrated in Fig. 1, we quantify the uncertainty ~~of resulting load predictions~~ in power and load predictions resulting from the *baseline*, *CS* and *WDS* simulations against results obtained with the *target* fields. The ~~*CS* and *WDS*~~ *CS* and *WDS* simulations are evaluated for the ~~analyzed~~ selected lidar configurations

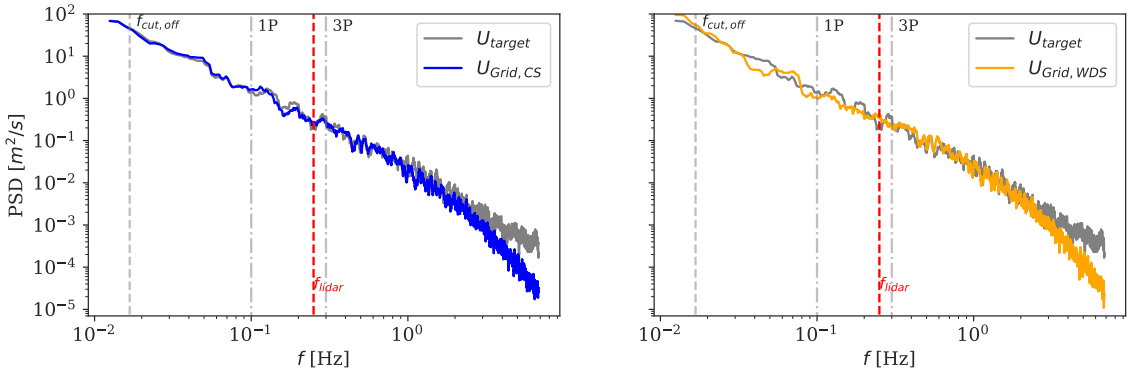

Figure 7. Comparisons of the power spectra density (PSD) of the ~~*target*~~ *target* u-velocity component measured at ~~hub-height~~ hub height with predictions obtained by the ~~*CS*~~*CS*-field (left) ~~,~~ and the ~~*WDS*~~*WDS*-field (right). The dominant frequency of the wake meandering $f_{cut,off} \approx 0.016$ Hz, the rotational frequency of the rotor and its harmonics (1P ≈ 0.1 Hz and 3P ≈ 0.3 Hz), and the Nyquist frequency of the lidar (≈ 0.25 Hz) are shown (see text for more details).

of Fig. 4, i.e., the 4P, 7P, Cone, SL, Grid and Grid* patterns with the parameters provided in Table 1. ~~Thus, the following~~ Two uncertainty indicators are ~~calculated~~defined to verify the load validation criteria *I* and *II* of Sect. 2:

- Bias: $\Delta_R = E(\tilde{y})/E(\hat{y})$,
- Uncertainty: $X_R = \sqrt{\langle(\tilde{y}/\hat{y} - E(\tilde{y})/E(\hat{y}))^2\rangle}$,

where the symbol $E(.)$ denotes the mean value and $\langle.\rangle$ the ensemble average, $\hat{y}$ is the quantity of interest (i.e., power or load statistics) derived from the *target* simulations, and $\tilde{y}$ corresponds to that produced by the reconstructed fields. We evaluate Δ_R and X_R on the resulting 10-min power and load statistics and provide results in Sect. 4.2.2 for the ~~*CS*~~*CS*-fields, and in Sect. 4.2.3 for the ~~*WDS*~~*WDS*-fields.

The analyzed wind turbine responses include mean power production levels ($\mathrm{Power}_{\mathrm{mean}}$), and fatigue loads. We ~~make use of~~ use the rainflow counting algorithm to compute the 1-Hz damage equivalent fatigue loads with a Wöhler exponent of m = 12 for blades and m = 4 for steel structures as tower and shaft. Thus, we compute fatigue loads at the blade root flapwise and edgewise moments $\mathrm{MxBR}_{\mathrm{DEL}}, \mathrm{MyBR}_{\mathrm{DEL}}$, tower-bottom fore-aft and side-side $\mathrm{MxTB}_{\mathrm{DEL}}, \mathrm{MyTB}_{\mathrm{DEL}}$, the torsional loads at the tower top (also referred to as yaw moment) $\mathrm{MzTT}_{\mathrm{DEL}}$ and torsional loads at the drivetrain $\mathrm{MzSh}_{\mathrm{DEL}}$.

Furthermore, we quantify the accuracy of the reconstructed wake fields based on estimates of the rotor-effective wind speed (U_{eff}), defined as the weighted sum of the u-velocity measured across the rotor area, the explained variance ratio ρ_E^2, and the u-velocity variance σ_u^2 computed from the reconstructed turbulence ~~boxes~~fields. Finally, a load time-series and spectral analysis is conducted in Sects. 4.2.4 and 4.2.5.

4.2.1 Site conditions

Load simulations are carried out using site-specific observations collected from the FINO1 meteorological mast installed at the German offshore wind farm Alpha Ventus. The wind farm is situated in the North Sea and about 45 km north of the island of Borkum (Kretschmer et al., 2019). Data were collected over a period of three years from 2011 to 2014~~and~~ , and their details can be found in Kretschmer et al. (2019).

In the present work, we only ~~make use of~~ use wind speeds and turbulence intensities measured ~~from a 90 m~~ under near-neutral conditions from a 90-m sonic anemometer installed at the mast. ~~Thus, we extract mean turbulence intensity~~ We extract 10-min average turbulence values binned for wind speeds ranging between 6 ~~m/s~~ and 22 m/s~~, under near-neutral conditions, and use these statistics as inputs for the load validation analysis. We use 18 turbulence seeds (the IEC recommends at least 6 seeds) for each wind speed in the range of 6–22 m/s, with a wind speed step of~~ ; using wind speed bins with 2 m/s ~~, and corresponding~~ we obtain nine bins with turbulence intensities of 8, 7, 7, 6, 6, 6, 6, 5, and 5%~~,~~. These are the statistics of the ambient wind field that we use as inputs for the load validation analysis.

For each 10-min sample of the inflow wind, we use 18 turbulence field realizations (the IEC 61400-1 recommends at least 6 realizations), leading to 162 aeroelastic simulations for each analyzed scanning configuration. Simulations with ambient wind speeds below 6 m/s are disregarded, as the wind speed approaching the rotor drops below the turbine's cut-in threshold ~~,~~ due to wake deficit effects, and the turbine shuts down.

Note that the recorded turbulence estimates at Alpha Ventus are considerably lower (approximately a factor of 3) than values recommended by the low turbulence IEC-class C. ~~Thus~~Here, we perform the load validation analysis on more realistic turbulence estimates characterizing offshore sites, since IEC-class C conditions would significantly attenuate the wake-induced effects, as higher ambient turbulence leads to a faster recovery of the wake deficit.

We use standard IEC-recommended turbulence ~~model parameters ($L = 29.4$ m and $\Gamma = 3.9$). The parameter~~ parameters for the Mann model (i.e., $L = 29.4$ m and $\Gamma = 3.9$ (IEC, 2019)), whereas $\alpha_k \epsilon^{2/3}$ is ~~fitted~~ tuned to obtain the ~~*target* turbulence levels in~~ *target* ambient turbulence levels of each simulation. The ~~atmospheric wind profile~~ inflow is described by a power-law with fixed shear exponent of ~~$\alpha = 0.2$~~$\alpha = 0.2$, as recommended in the IEC standard. The spacing between the analyzed and upstream turbines is fixed at 5 D. ~~Although we run the load validation procedure on selected nominal parameters, we investigate the sensitivity of the main load-driver parameters in a separate section (see Sect. 4.3).~~

The ~~*target*~~ *target* wake field characteristics ~~resulting~~ as function of the ambient wind speed, which result from the 162 simulations, are shown in Fig. 8. ~~It is seen that the~~ The wake considerably reduces the inflow wind speed approaching the rotor (i.e., U_{eff}) by ~~approximately~~ $\approx$ 35%, compared to the ambient wind speed ~~.~~ (see Fig. 8-**(a)**). This effect decreases for higher winds (> 14 m/s) due to the low thrust coefficients of the turbine~~. Further, the turbulence in the wake is~~ ; however, the wake deficit does not fully recover at high wind speeds, as we simulate relatively low ambient turbulence levels and the spacing between the turbines is short (i.e., 5 D).

Turbulence levels within the wake region are nearly doubled at low wind speeds compared to ~~ambient conditions. Finally~~the ambient conditions, as shown in Fig. 8-**(b)**. Further, the wake meandering ~~statistics~~ amplitudes, here computed as the standard

deviation of the wake center displacements in the ~~transversal directions normalized on~~ transverse directions normalized with the rotor diameter (σ_{μ_y}/D and σ_{μ_z}/D), are also shown ~~.~~ in Fig. 8-**(c),(d)**. As expected, larger wake displacements occur in the lateral than in the vertical directions (Keck et al., 2014; Machefaux et al., 2016).

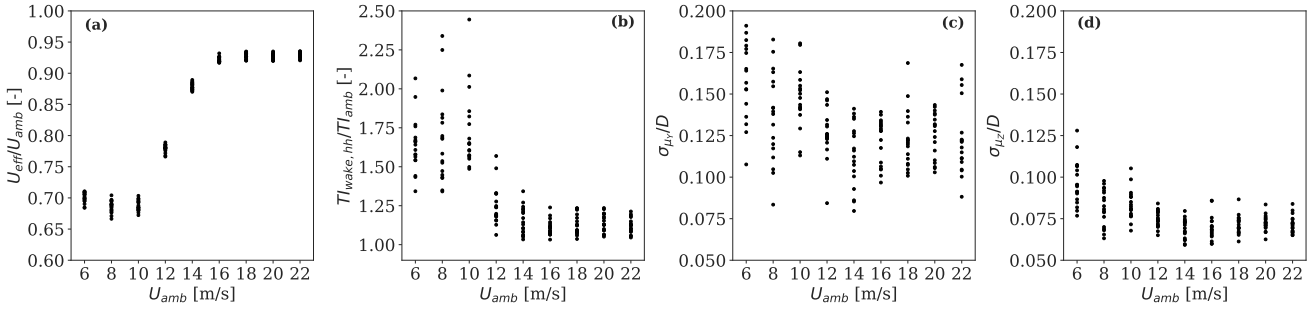

Figure 8. Scatter plots of the 10-min wake field characteristics resulting from the 162 simulations used as ~~*target*~~ *target* in the load analysis. The parameter $TI_{wake,hh}$ refers to the turbulence intensity measured at ~~hub-height~~ hub height in the wake; σ_{μ_y}/D is a measure of the amplitude of wake meandering in the lateral direction and σ_{μ_z}/D refers to the vertical displacement of the wake.

4.2.2 Load uncertainty of constrained Gaussian wake field simulations~~(CS)~~

~~The uncertainties~~

The uncertainties (Δ_R and X_R~~of the~~) of load predictions obtained with the ~~*CS*~~*CS*-fields as a function of the ambient wind speed are shown in Fig. 9. ~~It is found~~ We find that the biases largely vary depending on the simulated scanning pattern and analyzed load sensor. First, we ~~can observe that~~ observe that the patterns with fewer 'points' (i.e., 4P, 7P and Cone) overestimate U_{eff} by 2–10% (see Fig. 9a). This is because 1) these patterns ~~have insufficient spatial resolution to fully~~ scan an insufficient amount of positions within the inflow area to characterize the wake flow fully; 2) the autocorrelation structure of the unconstrained turbulence box is such that the spatial regions that are not scanned by the lidar are nearly uncorrelated with the locations of the imposed constraints~~. Thus, the reconstructed wind speed, ~~, as also shown in Fig. 5. Thus, in the regions that are not scanned by the lidar, the reconstructed wind speed approaches the ambient wind speed values. ~~Therefore~~

As a result, lower deficits are simulated, or equivalently higher rotor-effective wind speeds are predicted. ~~As a consequence~~Consequently, the power predictions are overestimated (Δ_R >10%), as seen for ambient wind speeds below 14 m/s in Fig. 9b. Patterns with high spatial resolution, as the SL, Grid, and Grid*, provide rotor-effective wind speed and power production estimates in good agreement with the ~~*baseline*~~*baseline*.

The statistics of ρ_E^2 in Fig. 9c indicate that increasing the ~~spatial resolution of the pattern~~ amount of points scanned by the lidar (see SL, Grid and Grid*) leads to a more accurate reconstruction of the wake turbulence. The biases of both ρ_E^2 and U_{eff} ~~decreases~~ decrease for high wind speeds ~~,~~ due to the attenuated wake-induced effects (see Fig. 8). The improved performance of the SL, Grid (and Grid*) is also confirmed by ~~the~~ estimates of σ_u^2 in Fig. 9d, which show that the SL and Grid configurations

can match the ~~target~~ *target* variance with an accuracy up to 98%, compared to 40–60% estimates inherent of the 4P, 7P, and the Cone configurations. Nevertheless, the observed biases of U_{eff}, ρ_E^2 and σ_u^2 reveal that the 4P, 7P, and Cone patterns lead to inaccurate wake field representations and do not satisfy the criteria of the load validation (see Criteria I in Sect. 2).

The results from simulations with the SL, Grid and Grid* patterns provide fatigue load statistics of $\mathrm{MxBR_{DEL}}$, $\mathrm{MxTB_{DEL}}$, $\mathrm{MzTT_{DEL}}$ and $\mathrm{MzSh_{DEL}}$ in good agreement with the results of the ~~baseline~~ *baseline* (see Fig. 9e–h). However, the calculated biases indicate a consistent underprediction at all wind speeds. This gap is largely compensated when probe volume effects are neglected, as seen for the Grid* (green lines). Overall, the observed deviations in the load predictions are due to the uncertainty of lidar measurements (i.e., size of the probe volume, cross-contamination effects, limited sampling frequency) ~~,~~ and the limited scanning coverage of the patterns.

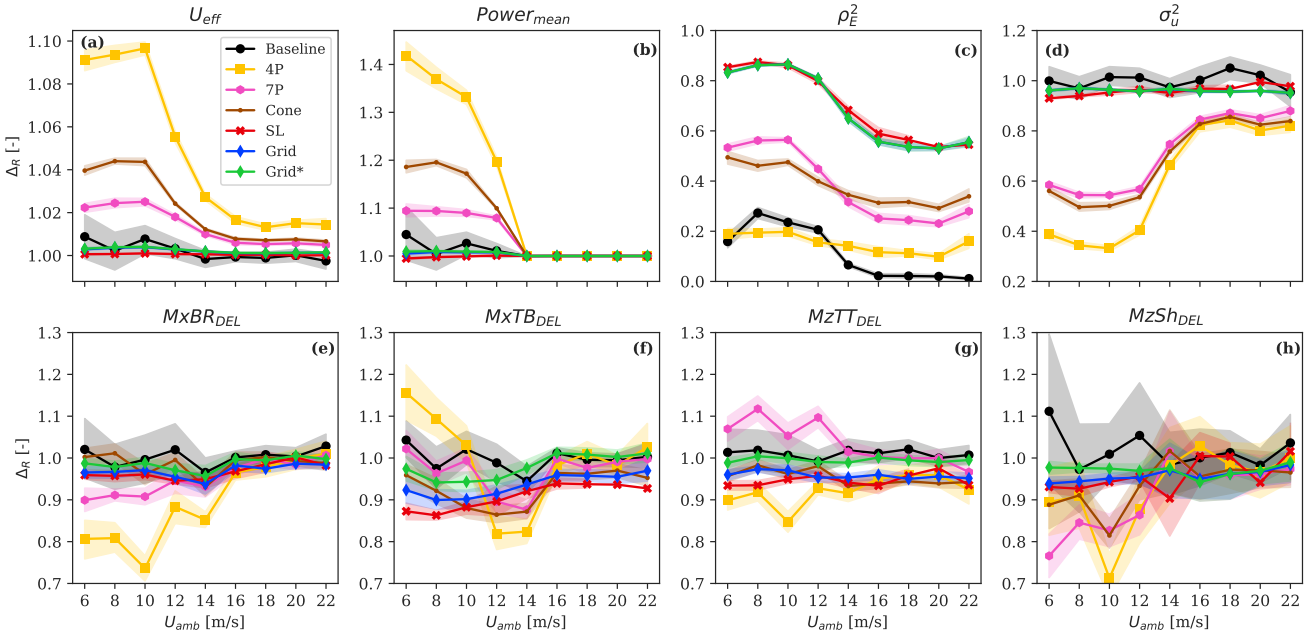

Figure 9. Comparison of bias Δ_R (solid line) and uncertainty X_R (error band) of selected load sensors as function of the ambient wind speed. The uncertainty indicators are computed against the ~~target~~ *target* observations, for each ambient wind speed (marker) that consists in 18 aeroelastic simulations with random turbulence seeds. The lidar-based results are derived from simulations with ~~CS~~*CS*-fields.

Figure 10 shows the statistics of Δ_R and X_R including all wind speeds. As expected, the ~~baseline~~ *baseline* leads to $\Delta_R \sim 1$ for all the analyzed load sensors, which indicates that the adopted 18 turbulence seeds are sufficient for the load statistics to converge. The large biases from simulations with the 4P, 7P, and Cone patterns ($\Delta_R \sim$0.87–1.37) follow from the inaccurate wind field reconstruction discussed above. The load predictions with the SL and the Grid configurations provide biases closer to the ~~baseline~~*baseline*, although turbulence-driven load sensors are underpredicted by 2–7%. These deviations decrease as

probe volume effects are neglected (i.e., $\Delta_R \sim 1\%$ for Grid* in Fig. 10-left), which shows the dependency of the load prediction accuracy on the probe volume size.

The statistics of X_R are shown in Fig. 10-right. The *baseline* baseline's X_R is a direct measure of the statistical uncertainty intrinsic of the DWM model, which is due to the stochastic properties of the synthetic turbulence field and wake meandering. Thus, the turbine responses that are largely affected by wake-induced effects are identified by high X_R values (see *baseline* baseline in Fig. 10-right). The power predictions as well as and the majority of fatigue loads show a relatively high statistical uncertainty ($X_R \sim 0.05$–0.09), resulting in a large load scatter.

The X_R values of MyTB and MzSh are significantly higher than other load sensors. The cause of the former is structural resonance occurring at low wind speeds that excites the tower natural frequency's natural frequency (Bak et al., 2013). This effect originates from a design aspect of the DTU 10 MW turbine, and it is independent of the wake-field reconstructing approach. The cause of the latter is the high X_R values of MzSh originate from the intense controller activity to regulate the generator torque under high-variable inflow conditions. The *CS*-based load predictions are characterized by significantly Significantly lower X_R values characterize the *CS*-based load predictions compared to the statistics obtained with the *baseline*. Indeed, *baseline*. X_R is values are reduced by a factor between 1.4–5 for the main wind driven wind-driven turbine responses such as $\text{Power}_{\text{mean}}$, and fatigue loads (i.e. MxBR_{DEL}, MxTB_{DEL}, MzTT_{DEL} and MzSh_{DEL}). The *CS* *CS*-fields, reconstructed using a sufficiently resolute scanning pattern and with scanning patterns with a sufficient amount of scanned positions and limited lidar probe volume can therefore , can satisfy both the load validation criteria stated Criteria I and II in Sect. 2.

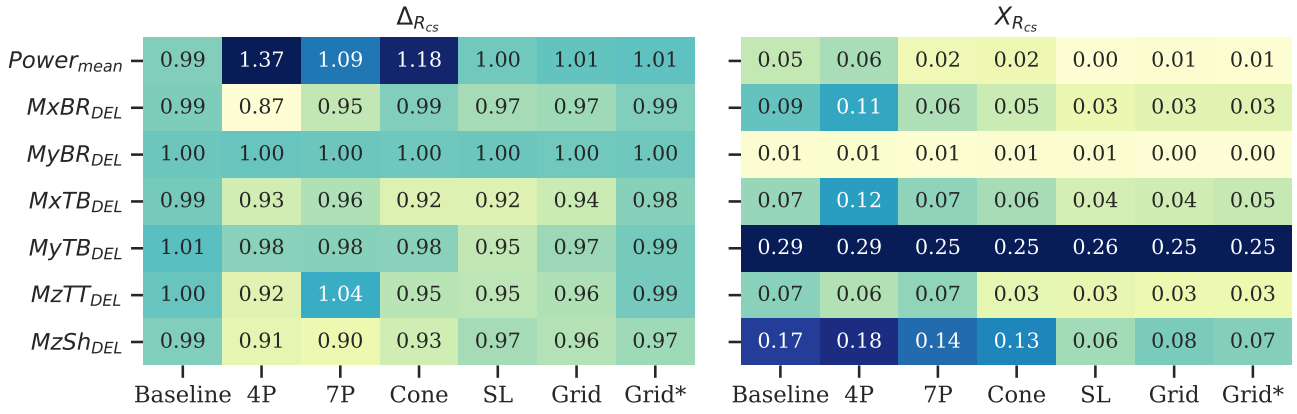

Figure 10. Uncertainty indicators of the load validation analysis based on the constrained field simulations (*CS* *CS*). Results are tabulated according to the load components and lidar scanning patterns. The color-map colormap reflects the amplitude of the error, thus a dark blue identifies an overprediction while the ligth-green indicates an underprediction. A perfect statistical prediction leads to $\Delta_R = 1$ and $X_R = 0$.

4.2.3 Load uncertainty of wake deficit superposition simulations~~(WDS)~~

We present the results relative to the ~~*WDS*~~ *WDS* simulations in the same fashion as ~~done for the *CS*~~ for the *CS* in Sect. 4.2.2. Thus, we plot the load ~~predictions uncertainty as~~ prediction uncertainty as a function of the ambient wind speeds in Fig. 11. ~~It can be noticed that the~~ The 4P, 7P and Cone patterns lead to improved biases of U_{eff}, and consequently $\mathrm{Power}_{\mathrm{mean}}$ (see Fig. 11a,b) ~~,~~ compared to the results obtained with the ~~*CS* fields (see~~ *CS* fields (shown in Fig. 10). ~~Indeed, the~~ The $\mathrm{Power}_{\mathrm{mean}}$ predictions computed with the ~~*WDS*~~*WDS*-approach and the 7P pattern are comparable with the ~~*baseline*~~*baseline*, while the ~~corresponding results with the *CS*~~results using the *CS*-fields ~~produced an overprediction of~~ overpredicted it by $\approx$ 10%. ~~In addition~~Also, improved estimates of both ρ_E^2 and σ_u^2 are ~~seen~~ found in Fig. 11c,d, and for low wind speeds, which indicates a more accurate reconstruction of the wake turbulence by the ~~*WDS*~~*WDS*- than the ~~*CS*~~*CS*-approach. In contrast, we find lower values of ρ_E^2 and σ_u^2 under higher compared to lower wind speeds because of the less pronounced wake deficits of the *target* fields, as also shown in Fig. 8-left.

These findings suggest that ~~, for patterns with low spatial resolution, more information of~~ more details on the wake characteristics ~~can be~~ are better recovered by fitting a ~~generic wake shape~~ wake deficit function rather than incorporating lidar measurements directly into the turbulence boxes, when looking at patterns where the inflow is scanned at few positions. Overall, simulations with the 7P, SL, Grid, and Grid* patterns can produce power predictions comparable with the ~~*baseline*~~ *baseline* (see Fig. 11b), whereas the 4P and Cone patterns lead to inaccurate predictions. Figure 11e – h shows that the fatigue loads obtained with the 7P, SL, Grid, and Grid* configurations are generally lower than ~~that from the *baseline*~~those from the *baseline*.

We quantify the statistics of Δ_R and X_R, including all the wind speeds ~~with *WDS*~~using *WDS*-simulated fields, and present the results in Fig. 12. As discussed above, the 4P and Cone patterns overpredict the rotor-effective wind speed and underpredict the wake turbulence; these effects counteract each other leading to fictitious biases of fatigue loads. Similar conclusions can be made for the 7P configuration, although it provides reliable power estimates.

As seen for the ~~*CS*~~*CS*-results, the SL, Grid, and Grid* configurations provide biases in good agreement with the ~~*baseline*~~*baseline*, although fatigue loads are underpredicted by $\Delta_R \sim$ 2–3%. By neglecting ~~the~~ volume-averaging effects (~~see~~ i.e., Grid*), only a marginal improvement of the biases is achieved. Simulations with the ~~*WDS*~~*WDS*-fields can reduce the statistical uncertainty of $\mathrm{Power}_{\mathrm{mean}}$ by a factor of 5 ~~, and~~ and that of the main load components (i.e., $\mathrm{MxBR}_{\mathrm{DEL}}$, $\mathrm{MxTB}_{\mathrm{DEL}}$, $\mathrm{MzTT}_{\mathrm{DEL}}$ and $\mathrm{MzSh}_{\mathrm{DEL}}$) by a factor of 1.2–2 compared to the $baseline$ (see X_R in Fig. 12-right).

4.2.4 Time-series analysis of load predictions

In this section, we investigate the accuracy of lidar-reconstructed load time-series against ~~*target*~~ *target* observations. An illustrative example is provided in Fig. 13, where the lidar-based power and loads time-series predictions are compared with the ~~*target* simulations. It is observed that both *CS*~~*target* simulations. As shown, both *CS*- and ~~*WDS*~~*WDS*-approaches ~~can~~ recover to a large extent wake-induced effects ~~,~~ and the instantaneous events on the wind turbine responses, leading to load

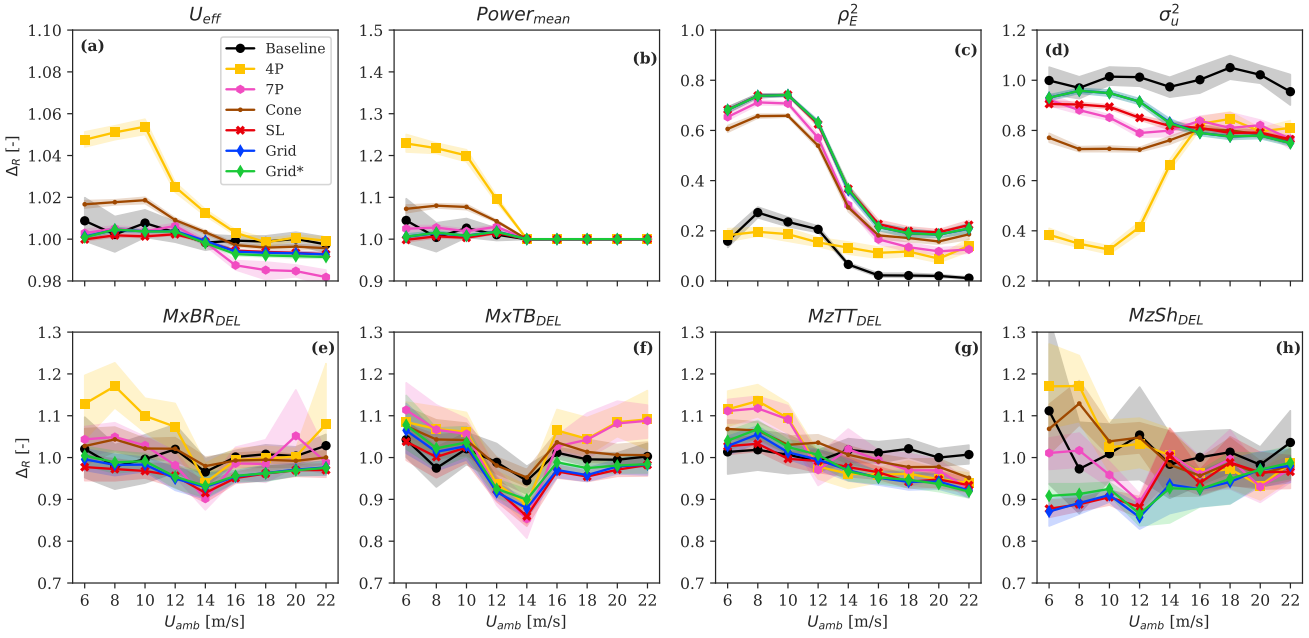

Figure 11. ~~Similar to Fig~~Comparison of bias Δ_R (solid line) and uncertainty X_R (error band) of selected load sensors as function of the ambient wind speed. ~~9 but~~ The uncertainty indicators are computed against the *target* observations, for ~~*WDS* fields~~each ambient wind speed (marker) that consists in 18 aeroelastic simulations with random turbulence seeds. The lidar-based results are derived from simulations with *WDS*-fields.

time-series that are highly correlated with the ~~*target*~~ *target* observations. This finding explains the reductions of X_R observed in Figs. 10 and 12.

In order to quantify the accuracy of the predicted load time-series, we evaluate the cross-correlations ~~measure~~ $\rho(\tilde{y},\hat{y}) = \mathrm{cov}(\tilde{y},\hat{y})/\sigma_{\tilde{y}}\sigma_{\hat{y}}$ ~~,~~between the lidar-based results ($\tilde{y}$) and the ~~*target*~~ *target* simulations ($\hat{y}$) (ρ = 1 means perfect correlation). We focus the analysis on the SL, Grid and Grid* configurations, which provide the most promising results, as demonstrated in the previous sections.

We compute ρ for all the 162 simulations and for each load component, and provide average estimates in Fig. 14. ~~It is found~~ We find that both the ~~*CS*~~*CS*- and ~~*WDS*~~*WDS*-predicted $\mathrm{Power}_{\mathrm{mean}}$ time-series reach a nearly perfect correlation with the actual ~~*target* observations (ρ = 0.96~~*target* observations (ρ = 0.96–0.99). Note that $\mathrm{Power}_{\mathrm{mean}}$ is a low frequency signal (see Fig. 13~~a~~), which is marginally affected by the local turbulence fluctuations. A high correlation value is also obtained for MxBR (ρ = 0.89ρ = 0.89–0.98), and for the tower top and shaft load components (ρ = 0.60ρ = 0.60–0.90).

The correlation relative to MxTB drops to ≈ 0.33 with the ~~*WDS*~~*WDS*-simulations, while higher values are achieved by the ~~*CS*~~ *CS* results. It should be noted that the structural resonance occurring at low wind speeds, which excites the tower can potentially affect the correlation results ~~. It can be seen from Fig. 13~~ (Bak et al., 2013). Figure 13 shows that the MxTB

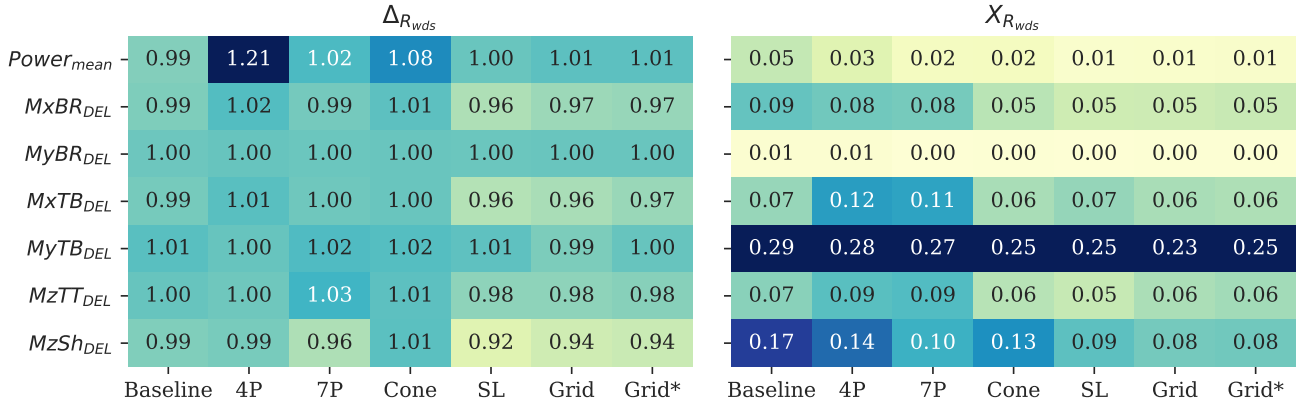

Figure 12. ~~Similar~~ Uncertainty indicators of the load validation analysis based on the wake deficit superposition simulations (*WDS*). Results are tabulated according to ~~Fig~~the load components and lidar scanning patterns. ~~10 but for *WDS* fields~~The color-map reflects the amplitude of the error, thus a dark blue identifies an overprediction while the ligth-green indicates an underprediction. A perfect statistical prediction leads to $\Delta_R = 1$ and $X_R = 0$.

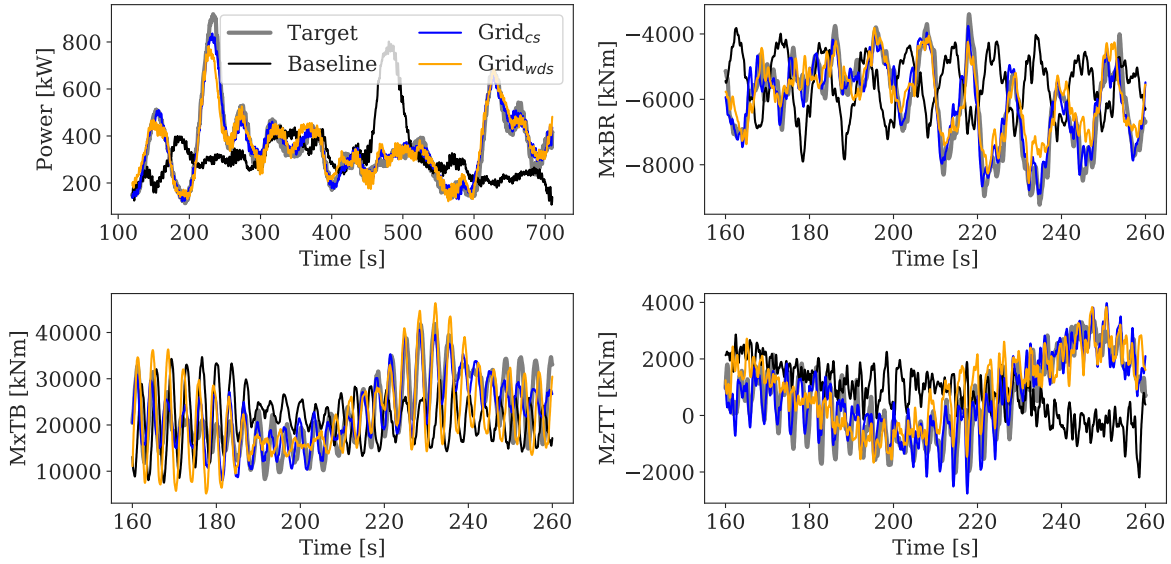

Figure 13. Comparison of predicted load time-series based on aeroelastic simulations carried out with the ~~*target*~~*target*, ~~*baseline*~~*baseline*, ~~*CS*~~*CS*- and ~~*WDS*~~*WDS*-reconstructed fields. The lidar-based fields are reconstructed using the Grid pattern.

time-series presents a nearly periodic signal, where the wind turbulence imprint is marginal. Overall, the accuracy of lidar-reconstructed load time-series show a significantly higher degree of correlation with the ~~*target*~~ *target* observations, compared

to that achieved by the ~~*baseline*~~*baseline*. Furthermore, the ~~*CS*~~*CS*-approach can predict more accurately the observed load fluctuations compared to the ~~*WDS*~~*WDS*-approach.

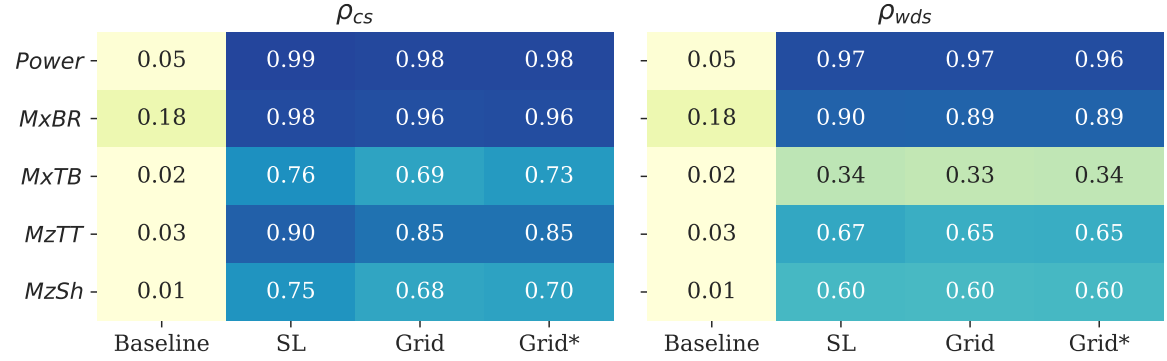

Figure 14. Average cross-correlation coefficient (ρ) computed between the reconstructed and ~~*target*~~ *target* load times-series from all the 162 simulations. Results from the ~~*CS*~~*CS*-fields are shown in the left panel, and ~~that~~ those from the ~~*WDS*~~*WDS*-fields in the right.

4.2.5 Spectral coherence analysis of load predictions

We conduct a spectral analysis on the time-series of MxBR, MxTB, and MzTT, which are highly correlated with the wake meandering (Muller et al., 2015; Moens et al., 2019; Ning and Wan, 2019) and are ~~largely affected by the~~ primarily affected by wake turbulence. The PSD analysis is provided in Appendix A ~~,~~and shows that neither of the wake field reconstruction methods ~~shifts~~ shift the energy content among ~~frequency~~ frequencies nor introduce instabilities (i.e., artificial artifacts).

The spectral coherence analysis provides more insight on the accuracy of reconstructed blade and tower loads. Here, we compute the coherence as ~~$\gamma = |S(\tilde{y},\hat{y})(f)|/(S(\tilde{y})(f)S(\hat{y})(f))$~~$\gamma^2 = |S(\tilde{y},\hat{y})(f)|^2/(S(\tilde{y})(f)S(\hat{y})(f))$, where $S(\tilde{y})$ and $S(\hat{y})$ are the auto-spectra of the ~~*CS* (or *WDS*) and *target*~~ *CS* (or *WDS*) and *target* load estimates, and $S(\tilde{y},\hat{y})$ is their cross-spectrum. We compare the coherence resulting from the load time-series produced by either ~~*CS* and *WDS* simulations and the *target* observations , at~~ *CS* and *WDS* simulations with the *target* observations for U_{amb} = 6 m/s and TI_{amb} = 8% ~~in~~ (see Fig. 15~~.~~).

It is observed that both field reconstruction techniques lead to high coherence in the proximity of the principal load frequencies, such as the rotational (1P for the blade, and 3P for the tower, see Fig. A1 for more details), the natural frequency of the tower ($\approx$ 0.25 Hz, which is close to the 3P at 6 m/s), and the dominant wake meandering frequency ($\approx$ 0.016 Hz). In general, the coherence from the ~~*CS*~~ *CS* simulations is non-zero at ~~frequency~~ frequencies up to 0.7 Hz (6P) ~~,~~and is higher ~~compared to that from *WDS*~~ than that from *WDS* simulations. This confirms that higher frequency fluctuations can be reconstructed more accurately using the ~~*CS*~~ *CS* approach.

By increasing the ~~spatial and temporal resolutions of the scanning pattern~~scanning pattern's temporal resolution and the number of scanned points, and neglecting volume-averaging effects, the ~~*CS*~~*CS*-approach could potentially reconstruct the

whole spectrum of the loads. ~~This presents a limitation of the *WDS*~~With the *WDS*-approach, ~~which only reconstructs~~ we can only reconstruct turbulence structures corresponding to the size of the wake deficit. Finally, given the limitation of the reconstruction techniques to recover small-scale turbulence structures, as discussed in Fig. 7, the accuracy of tower loads, which are driven by high-frequency fluctuations (see Fig. A1), ~~drops~~ is lower compared to that of the blades. This can partly explain the larger deviations of Δ_R, X_R and ρ, inherent of $\mathrm{MxTB_{DEL}}$ and relative to $\mathrm{MxBR_{DEL}}$, observed in Figs. 10, 12 and 14, as well as ~~the evidence that~~ explaining why Δ_R ~~of the~~ for $\mathrm{MxTB_{DEL}}$ ~~is the most improved~~ improves the most when the probe volume size is neglected, as seen in Fig. 10.

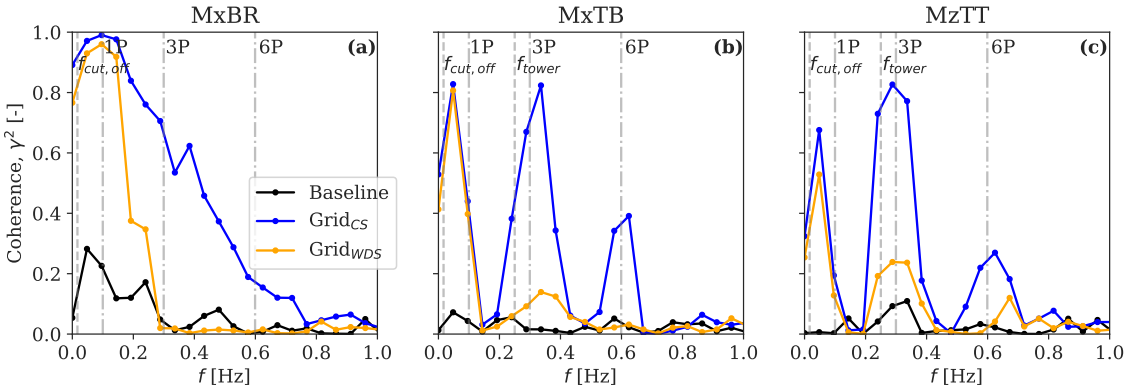

Figure 15. Spectral coherence analysis between the lidar-based load predictions and the ~~*target*~~ *target* simulations for **(a)** the blade root flapwise bending moment MxBR, **(b)** tower bottom fore-aft bending moment MxTB, and **(c)** yaw moment MzTT. The ~~*target*~~ *target* simulations are run for U_{amb} = 6 m/s and TI_{amb} = 8%. The ~~*baseline*~~*baseline*'s results are also shown in ~~dashed~~ solid black line, together with the principal operational frequencies of the wind turbine (1P ≈ 0.1 Hz, 3P and 6P) in dash-dot grey lines, the dominant frequency of the wake meandering $f_{cut,off} \approx 0.016$ Hz, and the natural frequency of the tower $f_{tower} \approx 0.25$ Hz in dashed grey lines.

4.3 Sensitivity analysis

The load validation of Sect. 4.2 is carried out using statistics collected under near-neutral conditions at Alpha Ventus, i.e., low atmospheric turbulence. Nevertheless, atmospheric turbulence conditions ~~has~~ have a strong impact on the wake development (Kumer et al., 2017; Zhan et al., 2020), and wind turbine loads (Sathe et al., 2013; Kretschmer et al., 2018). Further, the lidar measuring characteristics can impact the accuracy of reconstructed fields (Lundquist et al., 2015), thus that of load predictions. In the next subsections, we investigate the sensitivity of atmospheric turbulence conditions as well as selected lidar specifications on the accuracy of lidar-based load predictions using the Grid pattern as an example.

4.3.1 Effect of atmospheric turbulence conditions on load prediction accuracy

Figure 16a shows the sensitivity of the lidar-based load predictions bias ~~for~~ on TI_{amb} within the range 4–20%. The high TI_{amb} leads to faster recovery of the velocity deficit (Doubrawa et al., 2019), amplifies the wake meandering (Machefaux et al., 2016), and affects the accuracy of lidar-reconstructed fields (Pettas et al., 2020). This has a negligible effect on the accuracy of load predictions obtained with the ~~CS~~CS-fields, while larger deviations are observed for the ~~WDS~~ WDS results. This is partly due to the limited scanned area by the lidar combined with the large wake displacements. ~~Indeed, the~~ The fitting procedure intrinsic of the ~~WDS~~ WDS approach can lead to an inaccurate estimation of the wake shape parameters ~~,~~when the wake moves out of the scanned area (Trujillo et al., 2011).

We investigate the influence of the atmospheric turbulence length scale on the load prediction accuracy in Fig. 16b, by varying L between 5 and 70 m. Earlier studies have shown the strong dependency of load statistics on the turbulence length scales ~~(Sathe et al., 2013; Dimitrov et al., 2017; Conti et al., 2020a)~~(Sathe et al., 2013; Dimitrov et al., 2017; Conti et al., 2020b). Further, L provides a measure of the ~~resolution of the scanning configuration~~ scanning configuration resolution useful for performing constraints (Dimitrov and Natarajan, 2017).

The turbulence length scale affects the predicted statistics of the explained variance ratio of the ~~CS~~CS-fields, which decreases from ~~$\rho^2_E \sim$~~ $\rho^2_E \sim 0.8$ for ~~L = 29 m to $\rho^2_E \sim$~~ $L = 29$ m to $\rho^2_E \sim 0.6$ for ~~$L = 5$~~ $L = 5$ m (not shown). This indicates that when L is low, the turbulence structure sizes fall below the sampling fidelity of the ~~CS~~ CS approach (note that ~~a spatial resolution of~~ the scanned points of the Grid configuration are separated by 29 ~~m is assumed for the Grid~~ m as described in Sect. 3.3). The ~~biases of the CS~~CS-based load predictions' biases show a dependency on the turbulence length scales, while the ~~WDS~~WDS-fields are not significantly affected (see Fig. 16b).

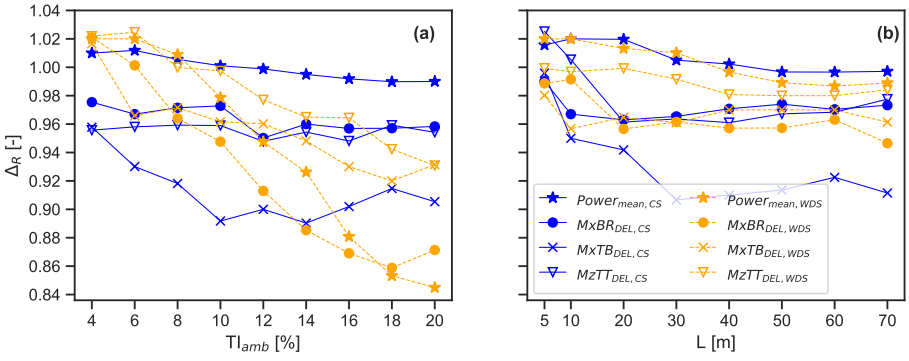

Figure 16. Influence of atmospheric turbulence conditions on the lidar-based load prediction accuracy, including: **(a)** the effect of ambient turbulence (T_{amb}) given U_{amb} = 6 m/s, **(b)** the effect of turbulence length scale, L, given U_{amb} = 6 m/s and TI_{amb} = 8%. The bias Δ_R at each nominal value is computed from 18 simulated seeds. The Grid pattern is used for the analysis.

4.3.2 Effect of lidar probe volume and scanning period on load prediction accuracy

One of the main limitations of ~~CW~~ continuous-wave lidars is that the probe volume size increases proportionally with the square of the focal distance (Sathe and Mann, 2013). As the diameter of modern wind turbines has reached ~~200 m, as for the DTU 10 MW,~~ 150–200 m, measuring at farther distances upfront of the rotor becomes an issue due to the larger probe volumes. Hence, we investigate the sensitivity of the lidar probe volume on the load prediction accuracy in Fig. 17a, by varying the probe volume length between 0 to 210 m. ~~It is seen that~~

As shown, the magnitude of Δ_R decreases almost linearly with increasing probe volume lengths. Further, the probe volume effects are more pronounced for the ~~*CS*~~*CS*-approach, which directly incorporates the low-pass filtered wind speed fluctuations into the reconstructed field.

Another limitation inherent of the ~~PL~~ pulsed lidar technology is the reduced sampling frequency compared to ~~CW~~ continuous-wave lidars (Peña et al., 2015). The ~~sensitivity of the~~ lidar sampling frequency sensitivity on the load prediction accuracy is assessed by varying the scanning period, which is defined as the time to complete a full scan (1–30 s). For this particular analysis, the ~~*target*~~ *target* simulations are run for U_{amb} = 6 m/s and TI_{amb} = 16%.

Although the scanning period does not play an important contribution to the load prediction accuracy, as shown in Fig. 17-b, this outcome is conditional to the dominant frequency of the wake meandering, which in turn decreases with larger rotors ($f_{cut,out} = U_{amb}/(2D)$), and the ~~spatial resolution of the pattern. The *CS*~~amount of scanned points in the inflow. The *CS*-results show that ~~accurate power predictions are obtained up to a scanning period~~ a bias lower than 2% in power predictions is found for scanning periods up to ≈20 s, which corresponds to ~~one third~~ one-third of the wake meandering dominant period.

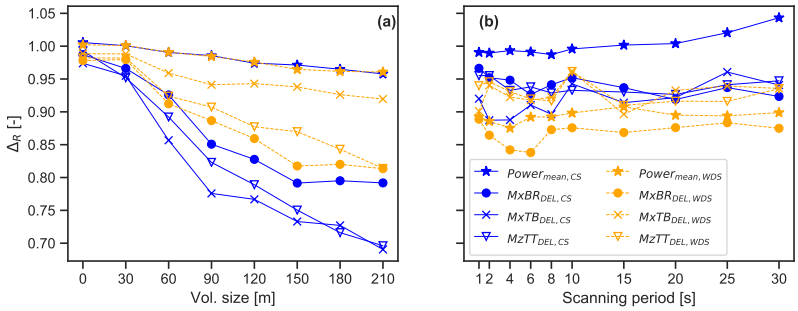

Figure 17. Influence of lidar scanning specifications on the lidar-based load prediction accuracy, including: **(a)** the effect of probe volume size given U_{amb} = 6 m/s and TI_{amb} = 8%, **(b)** the effect of the scanning period given U_{amb} = 6 m/s and TI_{amb} = 16%. The bias Δ_R at each nominal value is computed from 18 simulated seeds. The Grid pattern is used for the analysis.

5 Discussion

~~This study addresses the need for reducing the statistical load prediction uncertainty of wind turbines operating in wake conditions by incorporating lidar measurements in the wake field reconstruction.~~

One of the main elements used in the study is to consider as ~~*target*~~ *target* the wake flow fields generated by the DWM model. The DWM model is a simplified engineering wake model subjected to modelling uncertainties. Although the ~~wake deficit~~ mean wind velocity and turbulence fields in the far wake region can deviate from high-fidelity simulations ~~,~~ (e.g., computational fluid dynamics, CFD) or field data, the calibration of the DWM model coefficients can considerably improve the accuracy and provide ~~quasi-steady wake characteristics~~ wake fields in good agreement with lidar observations (Reinwardt et al., 2020) and CFD simulations (Keck et al., 2012, 2014, 2015). ~~This modelling uncertainty~~

The modelling uncertainty originated from an inaccurate calibration of the DWM model is not expected to significantly alter ~~the findings of this study~~this study's findings, as we demonstrate the robustness of the lidar-based approaches under a large variety of inflow wind and operational conditions. ~~Further, wake-added~~

The wake turbulence spectral properties are described, to the extent needed for the load analysis, by an isotropic Mann-generated turbulence field with a low length scale (Madsen et al., 2005). A more realistic modelling choice to accurately simulate the turbulence structures within the wake fields, which can also affect aeroelastic load simulations, is found in ~~large-eddy simulations (LES). In comparison to DWM simulated fields, the LES fields can potentially influence the load predictions (Churchfield et al., 2015; Nebenführ and Davidson, 2017), and the accuracy of reconstructed fields (Bauweraerts and Meyers, 2020) . Note that the~~ LES (Churchfield et al., 2015; Nebenführ and Davidson, 2017).

Further, lidar-based wind field reconstruction techniques applied to LES fields have been recently developed (Bauweraerts and Meyers, 2(. Nevertheless, the computational burden of high-fidelity simulations, such as LES, would make the statistical load analysis of this work unfeasible.

Another limitation stems from the lidar simulator used in the study, which replaces full-field lidar measurements. Real lidar data taken upfront the rotor should be corrected for induction (Borraccino et al., 2017; Mann et al., 2018), blade blockage effects, and wind evolution (Bossanyi, 2013; de Mare and Mann, 2016). These effects are not simulated due to the modeling assumptions of the DWM model ~~. In spite of the aforementioned limitations , this numerical framework allows us~~ and should be further investigated, e.g., using LES fields.

Despite the limitations mentioned above, the numerical framework developed within this work is useful to assess the influence of several uncertainty sources ~~and to~~ on power and load predictions and evaluate different lidar scanning strategies ~~under a variety of inflow wind conditions~~ in an idealized yet fully controllable environment.

~~The load analysis indicates that the field reconstruction techniques, lidar scanning strategies, and lidar's probe volume sizes have a significant influence on the accuracy of load assessment. Nevertheless, both the CS- and WDS-approaches can reconstruct to a large extent the wake dynamics that have the strongest impact on the power and load predictions. These include the spatial distribution of the velocity deficit and the added turbulence resulting from its motions in time. The lidar-based predicted load statistics are comparable to the results obtained with the IEC-recommended DWM model ($\Delta_R \sim 0.97 - 1.01$). Furthermore, the statistical uncertainty of the lidar-based load predictions is considerably reduced by a factor between 1.2–5 compared to DWM's results (the $baseline$). By combining lidar measurements with the CS- and WDS-reconstruction~~

approaches, we are able to simulate power and load time-series with strong similarities to the actual measured turbine responses, as shown in Sect. 4.2.4.

Yet, the characterization of the small scale Characterizing the small-scale wake-added turbulence poses a challenge given the current limitations of lidar's sampling frequency and probe volume size (Peña et al., 2017). The small scale small-scale wake-added turbulence enhances the energy spectral content in the high-frequency range, 1–20 0.4–20 Hz (Madsen et al., 2010; Chamorro et al., 2012; Singh et al., 2014), and its contribution on the fatigue damage varies according to the load component and turbine operational strategy (Tibaldi et al., 2015). Bergami and Gaunaa (2014) demonstrates that the strongest

Bergami and Gaunaa (2014) demonstrated that the most serious fatigue damage on the blades occurs at frequencies around 1P (0.1–0.16 Hz for the DTU 10 MW), whereas structures as tower top (nacelle) and tower bottom are mainly affected by the tower eigenfrequency ($\approx$ 0.25 Hz) and the 3P frequency (0.3–0.48 Hz). As the PSD of tower loads exhibits large energy spectral content at high frequencies (see Fig. A1), the accuracy of tower load predictions decreases compared to that achieved by blade loads, as seen found in Sects. 4.2.4 and 4.2.5.

We demonstrate that a high spatial resolution of the lidar scanning pattern number of lidar-scanned positions of the inflow is required to ensure an acceptable level of accuracy . Our in the reconstructed wake fields. The results reveal that the current commercially available nacelle-mounted lidars , here represented by (e.g., the 4P, 7P, and Cone patterns,) will not provide sufficient information to accurately reconstruct the wake fields for the purpose of the load validation in wakes. The accurately for the load assessments. In contrast, the scanning requirements are met by the SL, fulfilled by the SpinnerLidar and any arbitrary lidar that can potentially scan a greater region of the rotor, as for the here-simulated Grid e.g., a Grid-like configuration. Although we do not optimize the scanning strategies, it is inferred that the required spatial resolution number of positions scanned by the lidar depends on the size of the wake turbulence structures in the wind wake field.

It is observed that incorporating Incorporating a sufficient number of lidar measurements directly in the turbulence field can produce fields leads to more accurate load predictions , compared to assuming a generic functional shape of the wake deficit. This is shown by the time-series analysis in Sect. 4.2.4 and the spectral coherence analysis of Sect. 4.2.5, which illustrate that high frequency load fluctuations can be reconstructed more accurately by the CS- than the WDS-approach. Furthermore, the constrained field technique based on the Mann turbulence model can be extended to incorporate than assuming a wake deficit's generic shape function. The *CS* algorithm can also be extended to reconstruct the v- and w-turbulence fluctuations , as demonstrated in Dimitrov and Natarajan (2017)(Dimitrov and Natarajan, 2017). Additionally, the CS*CS*-method finds direct application for reconstructing more complex flow fields occurring in wind farms, e.g., multiple wakes.

The On the other hand, the accuracy of the WDS*WDS*-predicted loads is conditional to the goodness of the selected shape function's goodness to represent velocity deficits. The wake deficit can deviate from a Gaussian pattern shape as the atmosphere becomes more unstable (Ning and Wan, 2019), whereas it exhibits a double-peak shape in the near-wake region (Keck et al., 2014), and a more complex geometry in a multiple wake scenario. Our results show that combining a physical-based wake deficit formulation with actual lidar measurements of the Overall, reproducing the actual observed wake meandering path in the wake field simulations can potentially reduce the statistical uncertainty of power and load predictions. Overall, the

The fitting procedure of the ~~*WDS*~~*WDS*-approach is relatively fast and can provide ~~reliable~~ real-time ~~wake field estimates not only for load validation purposes, but also for improving~~ spatial and temporal characteristics of the wake flow field, which are useful for power and load predictions, wind farm monitoring, and control strategies. ~~On the other hand, the computational expenses of the *CS*-approach increase considerably with the amount~~ The computational cost of the *CS* algorithm considerably increases with the number of constraints simulated and the dimension of the turbulence boxes. For reference, a single wind field with 27900 constraints (i.e.~~SL~~, using the SL configuration) and a turbulence box with a grid size of $8192\times32\times32$ points currently ~~requires~~ require one and a ~~half hour~~ half-hour of simulation time on a single CPU.

6 Conclusions

This study proposed two alternative wind turbine load validation procedures under wake conditions that reconstruct synthetic wake fields from ~~time series~~ time-series of lidar retrievals. The first approach consisted ~~in incorporating lidar data~~ of incorporating nacelle lidar measurements of the wake ~~field directly~~ as constraints into random Mann turbulence field realizations. The second approach relied on the superposition of lidar-fitted bivariate Gaussian wake deficit time-series into the Mann turbulence fields.

~~We developed a numerical~~ The two approaches were numerically evaluated, adopting a tailored-designed framework that uses a virtual lidar simulator to scan ~~synthetic wake flow~~ three-dimensional wake fields simulated by the DWM model ~~, which were referred to as the actual *target* fields.The virtual lidar data were provided as input to the field reconstruction approaches.Thus, we carried out aeroelastic simulations with the lidar-reconstructed wake fieldsand quantified the load predictions uncertainty against results obtained with the *target*~~(i.e., the *target* fields).

~~It was found~~ We demonstrated that lidar-reconstructed ~~fields can potentially recover~~ wake fields recovered the main wake ~~characteristics influencing~~ flow features affecting wind turbine power and load predictions, such as the spatial distribution of the velocity deficit and its ~~dynamics within the simulated fields. This led to mean power and fatigue load estimates comparable with predictions of the DWM model ($\Delta_R \sim 0.97 - 1.01$), and a significant reduction of the~~ meandering dynamics. However, the accuracy of power and load estimates was highly conditional on the amount of scanned points by the lidar, the probe volume size, and the ambient turbulence intensity that in turn affected the wake evolution.

The load validation analysis showed that the current commercially available nacelle-mounted lidars would not provide sufficient spatial resolution to characterize wakes for power and load assessments, whereas research lidars, e.g., the SpinnerLidar and the Grid-like configuration, fulfilled these requirements.

Provided that a sufficient number of wind measurements were taken upwind of the rotor (e.g., using the SpinnerLidar or the Grid), incorporating them as constraints into turbulence fields was the most robust and accurate procedure for reconstructing wake fields and predicting power and loads. The lidar-reconstructed wake fields produced power and load time-series that were highly correlated with the *target* turbine responses; thus, reducing the statistical uncertainty (realization-to-realization) by a factor 1.2–5 ~~. The reduced statistical uncertainty was explained by improved predictions of power and load time-series, which~~

showed a high degree of correlation with the *target* turbine responses ($\rho \sim 0.33$–$0.99$when compared to the traditional load validation procedure (i.e., using the DWM model).

It was also demonstrated that the accuracy of the load predictions is mainly conditional on the spatial resolution of the lidar's scanning pattern, the Although unbiased power productions were predicted, the SpinnerLidar- and Grid-based reconstructed wake fields underpredicted fatigue load estimates by 1–8% depending on the load component and the size of the probe volume, and the adopted field reconstruction technique. . The biases in fatigue load predictions were reduced to less than 2% when neglecting probe volume effects.

Further investigations should validate the here-proposed approaches with evaluate the effects of rotor induction and turbulence evolution on the lidar-reconstructed wake fields' accuracy. Further, the proposed wake field reconstruction techniques should be validated using full-field data collected in operating wind farms.

Code availability.

Data availability.

Code and data availability.

Sample availability.

Video supplement.

Appendix A: Power Spectral Density (PSD) of load predictions

Figure A1 shows a comparison of the PSD of MxBR, MxTB, and MzTT between the lidar-reconstructed and ~~*target* simulations run at~~ *target* simulations for U_{amb} = 6 m/s and TI_{amb} = 8%. Figure A1a displays the PSD of MxBR, where the first three peaks correspond to the subsequent rotor harmonics (1P, 2P and 3P). The highest observed peak is at 1P ($\sim$ 0.1 Hz), which indicates that the greatest load cycle amplitude is due to asymmetric blade loading condition. This effect is amplified by the ~~in-homogeneous~~ inhomogeneous wake field approaching the rotor.

Compared to the rotating blades, the PSD of the tower loads MxTB and MzTT exhibits the largest energy content at higher frequencies ~~(>~~ up to 3P ($\sim$ 0.3 Hz). Further, the natural frequency of the tower (0.25 Hz) corresponds nearly to the 3P frequency at 6 m/s. This explains the very high peak seen for the MxTB. Overall, the PSD produced by the simulations with

lidar-reconstructed fields (CS and WDS) shows good agreement with that of the $target$ simulations, meaning that the energy content is not being shifted between frequencies. However, it is observed that the energy content at high frequency (> 1 Hz), induced by the wake-added turbulence, is not fully recovered due to the lidar probe volume and limited sampling frequency.

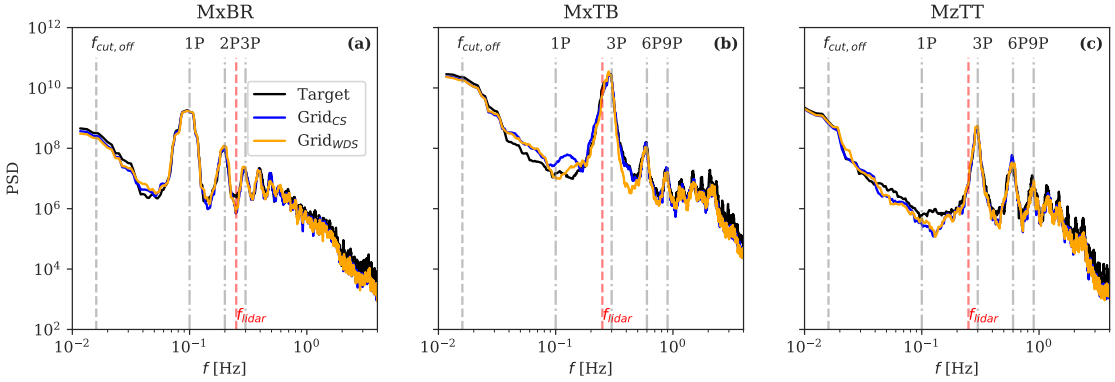

Figure A1. Power spectral density (PSD) of **(a)** the blade root flapwise bending moment MxBR, **(b)** tower bottom fore-aft bending moment MxTB, and **(c)** yaw moment MzTT. The dominant frequency of the wake meandering $f_{cut,off}$ = 0.016 Hz, the Nyquist frequency of the lidar f_{lidar} = 0.25 Hz (corresponding to the scanning period), and the main rotational frequencies 1P, 2P, 3P, 6P and 9P are shown. The $target$ simulations are run at 6 m/s with TI$_{amb}$ = 8%.

Author contributions.

Competing interests.

Disclaimer.

Acknowledgements. The work conducted by Vasilis Pettas is funded by the German Federal Ministry for Economic Affairs and Energy (BMWi) in the framework of the national joint research project RAVE - OWP Control (ref, 0324131B).

References

International Standard IEC61400-13: Wind turbines - Part 13: Measurement of mechanical loads, Standard, IEC, 2015.

International Standard IEC61400-12-1: Wind energy generation systems - Part 12-1: Power performance measurements of electricity producing wind turbines, Standard, IEC, 2017.

International Standard IEC61400-1: wind turbines—part 1: design guidelines, Fourth; 2019, Standard, IEC, 2019.

Achen, C. H.: Interpreting and Using Regression, Sage Publications, https://doi.org/https://dx.doi.org/10.4135/9781412984560, 1982.

Ainslie, J.: Calculating the flow field in the wake of wind turbines, Journal of Wind Engineering and Industrial Aerodynamics, 27, 213–224, https://doi.org/10.1016/0167-6105(88)90037-2, 1988.

Ainslie, J. F.: WAKE MODELLING AND THE PREDICTION OF TURBULENCE PROPERTIES, Proceedings of the Bwea Wind Energy Conference (british Wind Energy Association), pp. 115–120, 1986.

Bak, C., Zahle, F., Bitsche, R., Teaseong, K., Yde, A., LC, H., Natarajano, A., and Hansen, M.: Description of the DTU 10MW reference wind turbine, 2013.

Barthelmie, R. J., Hansen, K. S., Frandsen, S. T., Rathmann, O., Schepers, J., Schlez, W., Phillips, J., Rados, K., Zervos, A., Politis, E., and Chaviaropoulos, P.: Modelling and Measuring Flow and Wind Turbine Wakes in Large Wind Farms Offshore, Wind Energy, 12, 431–444, https://doi.org/10.1002/we.348, 2009.

Bauweraerts, P. and Meyers, J.: Bayesian based estimation of turbulent flow fields from lidar observations in a conventionally neutral atmospheric boundary layer, Journal of Physics: Conference Series, 1618, 032 047, https://doi.org/10.1088/1742-6596/1618/3/032047, 2020.

Bauweraerts, P. and Meyers, J.: Reconstruction of turbulent flow fields from lidar measurements using large-eddy simulation, Journal of Fluid Mechanics, 906, A17, https://doi.org/10.1017/jfm.2020.805, 2021.

Bergami, L. and Gaunaa, M.: Analysis of aeroelastic loads and their contributions to fatigue damage, Journal of Physics: Conference Series (online), 555, 012 007, https://doi.org/10.1088/1742-6596/555/1/012007, 2014.

Bingöl, F., Mann, J., and Larsen, G. C.: Light detection and ranging measurements of wake dynamics Part I: One-dimensional Scanning, Wind Energy, 13, 51–61, https://doi.org/10.1002/we.352, 2010.

Borraccino, A., Schlipf, D., Haizmann, F., and Wagner, R.: Wind Field Reconstruction from Nacelle-Mounted Lidars Short Range Measurements, Wind Energy Science, 2, 269–283, https://doi.org/10.5194/wes-2017-10, 2017.

Bos, R., Giyanani, A., and Bierbooms, W.: Assessing the severity ofwind gusts with lidar, Remote Sensing, 8, 758, https://doi.org/10.3390/rs8090758, 2016.

Bossanyi, E.: Un-freezing the turbulence: application to LiDAR-assisted wind turbine control, Iet Renewable Power Generation, 7, 321–329, https://doi.org/10.1049/iet-rpg.2012.0260, 2013.

Bossanyi, E. A., Kumar, A., and Hugues-Salas, O.: Wind turbine control applications of turbine-mounted LIDAR, Journal of Physics: Conference Series, 555, 012 011, https://doi.org/10.1088/1742-6596/555/1/012011, 2014.

Chamorro, L. P., Guala, M., Arndt, R. E., and Sotiropoulos, F.: On the evolution of turbulent scales in the wake of a wind turbine model, Journal of Turbulence, 13, 1–13, https://doi.org/10.1080/14685248.2012.697169, 2012.

Churchfield, M. J., Moriarty, P. J., Hao, Y., Lackner, M. A., Barthelmie, R., Lundquist, J. K., and Oxley, G. S.: A comparison of the dynamic wake meandering model, large-eddy simulation, and field data at the egmond aan Zee offshore wind plant, 33rd Wind Energy Symposium, pp. 20 pp., 20 pp., 2015.

Conti, D., Dimitrov, N., and Peña, A.: Aero-elastic load validation in wake conditions using nacelle-mounted lidar measurements, Wind Energy Science Discussions, 2020, 1–31, https://doi.org/10.5194/wes-2020-8, https://www.wind-energ-sci-discuss.net/wes-2020-8/, 2020a.

Conti, D., Dimitrov, N. K., and Peña, A.: Aeroelastic load validation in wake conditions using nacelle-mounted lidar measurements, Wind Energy Science, 5, 1129–1154, https://doi.org/10.5194/wes-5-1129-2020, 2020b.

de Mare, M. T. and Mann, J.: On the Space-Time Structure of Sheared Turbulence, Boundary-layer Meteorology, 160, 453–474, https://doi.org/10.1007/s10546-016-0143-z, 2016.

Dimitrov, N., Borraccino, A., Peña, A., Natarajan, A., and Mann, J.: Wind turbine load validation using lidar-based wind retrievals, Wind Energy, 22, 1512–1533, https://doi.org/10.1002/we.2385, 2019.

Dimitrov, N. K. and Natarajan, A.: Application of simulated lidar scanning patterns to constrained Gaussian turbulence fields for load validation, Wind Energy, 20, 79–95, https://doi.org/10.1002/we.1992, 2017.

Dimitrov, N. K., Natarajan, A., and Mann, J.: Effects of normal and extreme turbulence spectral parameters on wind turbine loads, Renewable Energy, 101, 1180–1193, https://doi.org/10.1016/j.renene.2016.10.001, 2017.

Dimitrov, N. K., Kelly, M. C., Vignaroli, A., and Berg, J.: From wind to loads: wind turbine site-specific load estimation with surrogate models trained on high-fidelity load databases, Wind Energy Science, 3, 767–790, https://doi.org/10.5194/wes-3-767-2018, 2018.

Doubrawa, P., Barthelmie, R. J., Wang, H., Pryor, S. C., and Churchfield, M. J.: Wind turbinewake characterization from temporally disjunct 3-D measurements, Remote Sensing, 8, 939, https://doi.org/10.3390/rs8110939, 2016.

Doubrawa, P., Barthelmie, R. J., Wang, H., and Churchfield, M. J.: A stochastic wind turbine wake model based on new metrics for wake characterization, Wind Energy, 20, 449–463, https://doi.org/10.1002/we.2015, 2017.

Doubrawa, P., Debnath, M., Moriarty, P. J., Branlard, E., Herges, T. G., Maniaci, D. C., and Naughton, B.: Benchmarks for Model Validation based on LiDAR Wake Measurements, Journal of Physics: Conference Series, 1256, 012 024, https://doi.org/10.1088/1742-6596/1256/1/012024, 2019.

Fuertes, F. C., Markfort, C. D., and Porteacute-Agel, F.: Wind Turbine Wake Characterization with Nacelle-Mounted Wind Lidars for Analytical Wake Model Validation, Remote Sensing, 10, 668 (18 pp.), 668 (18 pp.), https://doi.org/10.3390/rs10050668, 2018.

Held, D. P. and Mann, J.: Detection of wakes in the inflow of turbines using nacelle lidars, Wind Energy Science, 4, 407–420, https://doi.org/10.5194/wes-4-407-2019, 2019a.

Held, D. P. and Mann, J.: Lidar estimation of rotor-effective wind speed - An experimental comparison, Wind Energy Science, 4, 421–438, https://doi.org/10.5194/wes-4-421-2019, 2019b.

Herges, T. G. and Keyantuo, P.: Robust Lidar Data Processing and Quality Control Methods Developed for the SWiFT Wake Steering Experiment, Journal of Physics: Conference Series, 1256, 012 005, https://doi.org/10.1088/1742-6596/1256/1/012005, 2019.

Hoffman, Y. and Ribak, E.: Constrained realizations of Gaussian fields - A Simple algorithm, Astrophysical Journal, 380, L5–L8, https://doi.org/10.1086/186160, 1991.

Kaimal, J., Izumi, Y., Wyngaard, J., and Cote, R.: Spectral characteristics of surface-layer turbulence, Quarterly Journal of the Royal Meteorological Society, 98, 563, https://doi.org/10.1002/qj.49709841707, 1972.

Keck, R.-E., Veldkamp, D., Aagaard Madsen, H., and Larsen, G. C.: Implementation of a Mixing Length Turbulence Formulation Into the Dynamic Wake Meandering Model, Journal of Solar Energy Engineering, 134, 021 012, https://doi.org/10.1115/1.4006038, 2012.

Keck, R.-E., de Mare, M. T., Churchfield, M. J., Lee, S., Larsen, G. C., and Aagaard Madsen, H.: On atmospheric stability in the dynamic wake meandering model, Wind Energy, 17, 1689–1710, https://doi.org/10.1002/we.1662, 2014.

Keck, R. E., De Maré, M., Churchfield, M. J., Lee, S., Larsen, G., and Madsen, H. A.: Two improvements to the dynamic wake meandering model: Including the effects of atmospheric shear on wake turbulence and incorporating turbulence build-up in a row of wind turbines, Wind Energy, 18, 111–132, https://doi.org/10.1002/we.1686, 2015.

Kretschmer, M., Schwede, F., Faerron Guzmán, R., Lott, S., and Cheng, P. W.: Influence of atmospheric stability on the load spectra of wind turbines at alpha ventus, Journal of Physics: Conference Series, 1037, 052 009, https://doi.org/10.1088/1742-6596/1037/5/052009, 2018.

Kretschmer, M., Pettas, V., and Cheng, P. W.: Effects of wind farm down-regulation in the offshore wind farm Alpha ventus, Asme 2019 2nd International Offshore Wind Technical Conference, Iowtc 2019, https://doi.org/10.1115/IOWTC2019-7554, 2019.

Kristensen, L., Lenschow, D., Kirkegaard, P., and Courtney, M.: The Spectral Velocity Tensor for Homogeneous Boundary Layer Turbulence, Boundary-layer Meteorology, 47, 149–193, https://doi.org/10.1007/BF00122327, 1989.

Kumer, V. M., Reuder, J., and Eikill, R. O.: Characterization of turbulence in wind turbine wakes under different stability conditions from static Doppler LiDAR measurements, Remote Sensing, 9, 242, https://doi.org/10.3390/rs9030223, 2017.

Larsen, G., Ott, S., Liew, J., van der Laan, M., Simon, E., R.Thorsen, G., and Jacobs, P.: Yaw induced wake deflection - a full-scale validation study, Journal of Physics - Conference Series, 1618, 062 047, https://doi.org/10.1088/1742-6596/1618/6/062047, 2020.

Larsen, G. C., Madsen Aagaard, H., Bingöl, F., Mann, J., Ott, S., Sørensen, J., Okulov, V., Troldborg, N., Nielsen, N. M., Thomsen, K., Larsen, T. J., and Mikkelsen, R.: Dynamic wake meandering modeling, 2007.

Larsen, G. C., Madsen Aagaard, H., Thomsen, K., and Larsen, T. J.: Wake meandering: A pragmatic approach, Wind Energy, 11, 377–395, https://doi.org/10.1002/we.267, 2008.

Larsen, T. J. and Hansen, A. M.: How 2 HAWC2, the user's manual, Risø National Laboratory, 2007.

Larsen, T. J., Aagaard Madsen, H., Larsen, G. C., and Hansen, K. S.: Validation of the dynamic wake meander model for loads and power production in the Egmond aan Zee wind farm, Wind Energy, 16, 605–624, https://doi.org/10.1002/we.1563, 2013.

Lee, S., Churchfield, M., Moriarty, P., Jonkman, J., and Michalakes, J.: Atmospheric and wake turbulence impacts on wind turbine fatigue loadings, 50th Aiaa Aerospace Sciences Meeting Including the New Horizons Forum and Aerospace Exposition, pp. AIAA 2012–0540, https://doi.org/10.2514/6.2012-540, 2012.

Liew, J., Raimund Pirrung, G., and Meseguer Urbán, A.: Effect of varying fidelity turbine models on wake loss prediction, Journal of Physics: Conference Series, 1618, 062 002, https://doi.org/10.1088/1742-6596/1618/6/062002, 2020.

Lundquist, J. K., Churchfield, M. J., Lee, S., and Clifton, A.: Quantifying error of lidar and sodar doppler beam swinging measurements of wind turbine wakes using computational fluid dynamics, Atmospheric Measurement Techniques, 8, 907–920, https://doi.org/10.5194/amt-8-907-2015, 2015.

Lydia, M., Kumar, S. S., Selvakumar, A. I., and Prem Kumar, G. E.: A comprehensive review on wind turbine power curve modeling techniques, Renewable and Sustainable Energy Reviews, 30, 452–460, https://doi.org/10.1016/j.rser.2013.10.030, 2014.

Machefaux, E., Larsen, G. C., Koblitz, T., Troldborg, N., Kelly, M. C., Chougule, A. S., Hansen, K. S., and Rodrigo, J. S.: An experimental and numerical study of the atmospheric stability impact on wind turbine wakes, Wind Energy, 19, 1785–1805, https://doi.org/10.1002/we.1950, 2016.

Madsen, Helge Aagaard, H., Larsen, G. C., and Thomsen, K.: Wake flow characteristics in low ambient turbulence conditions, Proceedings (cd-rom), 2005.

Madsen, H. A., Larsen, G. C., Larsen, T. J., Troldborg, N., and Mikkelsen, R. F.: Calibration and Validation of the Dynamic Wake Meandering Model for Implementation in an Aeroelastic Code, Journal of Solar Energy Engineering, 132, 041 014, https://doi.org/10.1115/1.4002555, 2010.

Mann, J.: The spatial structure of neutral atmospheric surface-layer turbulence, Journal of Fluid Mechanics, 273, 141–168, 1994.

Mann, J., Pena Diaz, A., Bingöl, F., Wagner, R., and Courtney, M.: Lidar Scanning of Momentum Flux in and above the Atmospheric Surface Layer, Journal of Atmospheric and Oceanic Technology, 27, 959–976, https://doi.org/10.1175/2010jtecha1389.1, 2010.

Mann, J., Peña Diaz, A., Troldborg, N., and Andersen, S. J.: How does turbulence change approaching a rotor?, Wind Energy Science, 3, 293–300, https://doi.org/10.5194/wes-3-293-2018, 2018.

Medley, J., Barker, W., Harris, M., Pitter, M., Slinger, C., Mikkelsen, T., and Sjöholm, M.: Evaluation of wind flow with a nacelle-mounted, continuous wave wind lidar, Proceedings of Ewea 2014, 2014.

Moens, M., Coudou, N., and Philippe, C.: A numerical study of correlations between wake meandering and loads within a wind farm, Journal of Physics: Conference Series, 1256, 012 012, https://doi.org/10.1088/1742-6596/1256/1/012012, 2019.

Muller, Y. A., Aubrun, S., and Masson, C.: Determination of real-time predictors of the wind turbine wake meandering, Experiments in Fluids, 56, 1–11, https://doi.org/10.1007/s00348-015-1923-9, 2015.

Nebenführ, B. and Davidson, L.: Prediction of wind-turbine fatigue loads in forest regions based on turbulent LES inflow fields, Wind Energy, 20, 1003–1015, https://doi.org/10.1002/we.2076, 2017.

Nielsen, M., Larsen, G. C., Mann, J., Ott, S., Hansen, K. S., and Pedersen, B.: Wind Simulation for Extreme and Fatigue Loads, Risø National Laboratory, 2003.

Ning, X. and Wan, D.: LES study of wake meandering in different atmospheric stabilities and its effects on wind turbine aerodynamics, Sustainability (switzerland), 11, 6939, https://doi.org/10.3390/su11246939, 2019.

Pedersen, M. M., Larsen, T. J., Madsen, H. A., and Larsen, G. C.: More accurate aeroelastic wind-turbine load simulations using detailed inflow information, Wind Energy Science, 4, 303–323, https://doi.org/10.5194/wes-4-303-2019, 2019.

Pettas, V., García, F. C., Kretschmer, M., Rinker, J. M., Clifton, A., and Cheng, P. W.: A numerical framework for constraining synthetic wind fields with lidar measurements for improved load simulations, https://doi.org/10.2514/6.2020-0993, https://arc.aiaa.org/doi/abs/10.2514/6.2020-0993, 2020.

Peña, A., Hasager, C. B., Badger, M., Barthelmie, R. J., Bingöl, F., Cariou, J.-P., Emeis, S., Frandsen, S. T., Harris, M., Karagali, I., Larsen, S. E., Mann, J., Mikkelsen, T., Pitter, M., Pryor, S., Sathe, A., Schlipf, D., Slinger, C., and Wagner, R.: Remote Sensing for Wind Energy, 2015.

Peña, A., Mann, J., and Dimitrov, N. K.: Turbulence characterization from a forward-looking nacelle lidar, Wind Energy Science, 2, 133–152, https://doi.org/10.5194/wes-2-133-2017, 2017.

Peña, A., Mann, J., and Rolighed Thorsen, G.: SpinnerLidar measurements for the CCAV52, 2019.

Reinwardt, I., Schilling, L., Dalhoff, P., Steudel, D., and Breuer, M.: Dynamic wake meandering model calibration using nacelle-mounted lidar systems, Wind Energy Science, 5, 775–792, https://doi.org/10.5194/wes-5-775-2020, 2020.

Rettenmeier, A., Schlipf, D., Würth, I., and Cheng, P. W.: Power performance measurements of the NREL CART-2 wind turbine using a nacelle-based lidar scanner, Journal of Atmospheric and Oceanic Technology, 31, 2029–2034, https://doi.org/10.1175/JTECH-D-13-00154.1, 2014.

Rommel, D. P., Di Maio, D., and Tinga, T.: Calculating wind turbine component loads for improved life prediction, Renewable Energy, 146, 223–241, https://doi.org/10.1016/j.renene.2019.06.131, 2020.

Sathe, A. and Mann, J.: A review of turbulence measurements using ground-based wind lidars, Atmospheric Measurement Techniques, 6, 3147–3167, https://doi.org/10.5194/amt-6-3147-2013, 2013.

Sathe, A., Mann, J., Barlas, T. K., Bierbooms, W., and van Bussel, G.: Influence of atmospheric stability on wind turbine loads, Wind Energy, 16, 1013–1032, https://doi.org/10.1002/we.1528, 2013.

Schlipf, D., Schlipf, D. J., and Kuehn, M.: Nonlinear model predictive control of wind turbines using LIDAR, Wind Energy, 16, 1107–1129, https://doi.org/10.1002/we.1533, 2013.

Schreiber, J., Bottasso, C. L., Salbert, B., and Campagnolo, F.: Improving wind farm flow models by learning from operational data, Wind Energy Science, 5, 6472 020, https://doi.org/10.5194/wes-5-647-2020, 2020.

Simley, E., Pao, L. Y., Kelley, N., Jonkman, B., and Frehlich, R.: LIDAR wind speed measurements of evolving wind fields, 50th Aiaa Aerospace Sciences Meeting Including the New Horizons Forum and Aerospace Exposition, pp. AIAA 2012–0656, https://doi.org/10.2514/6.2012-656, 2012.

Simley, E., Y. Pao, L., Frehlich, R., Jonkman, B., and Kelley, N.: Analysis of Wind Speed Measurements using Continuous Wave LIDAR for Wind Turbine Control $_*$†, 2013.

Simley, E., Fürst, H., Haizmann, F., and Schlipf, D.: Optimizing lidars for wind turbine control applications-Results from the IEA Wind Task 32 workshop, Remote Sensing, 10, 863, https://doi.org/10.3390/rs10060863, 2018.

Singh, A., Howard, K. B., and Guala, M.: On the homogenization of turbulent flow structures in the wake of a model wind turbine, Physics of Fluids, 26, 025 103, https://doi.org/10.1063/1.4863983, 2014.

Tautz-Weinert, J. and Watson, S. J.: Using SCADA data for wind turbine condition monitoring - A review, Iet Renewable Power Generation, 11, 382–394, https://doi.org/10.1049/iet-rpg.2016.0248, 2017.

Tibaldi, C., Henriksen, L. C., Hansen, M. H., and Bak, C.: Wind turbine fatigue damage evaluation based on a linear model and a spectral method, Wind Energy, 19, 1289–1306, https://doi.org/10.1002/we.1898, 2015.

Trujillo, J.-J., Bingöl, F., Larsen, G. C., Mann, J., and Kühn, M.: Light detection and ranging measurements of wake dynamics. Part II: two-dimensional scanning, Wind Energy, 14, 61–75, https://doi.org/10.1002/we.402, 2011.

Wagner, R., Friis Pedersen, T., Courtney, M., Antoniou, I., Davoust, S., and Rivera, R.: Power curve measurement with a nacelle mounted lidar, Wind Energy, 17, 1441–1453, https://doi.org/10.1002/we.1643, 2014.

Wagner, R., Courtney, M. S., Friis Pedersen, T., and Davoust, S.: Uncertainty of power curve measurement with a two-beam nacelle-mounted lidar, Wind Energy, 19, 1269–1287, https://doi.org/10.1002/we.1897, 2015.

Zhan, L., Letizia, S., and Valerio Iungo, G.: LiDAR measurements for an onshore wind farm: Wake variability for different incoming wind speeds and atmospheric stability regimes, Wind Energy, 23, 501–527, https://doi.org/10.1002/we.2430, 2020.

Zwick, D. and Muskulus, M.: The simulation error caused by input loading variability in offshore wind turbine structural analysis, Wind Energy, 18, 1421–1432, https://doi.org/10.1002/we.1767, 2015.